JEM Journal of Experimental Medicine

ARTICLE

Synaptic pruning of murine adult-born neurons by microglia depends on phosphatidylserine

Chihiro Kurematsu[1], Masato Sawada[1,2], Masaki Ohmuraya[3], Motoki Tanaka[4], Kazuya Kuboyama[1], Takashi Ogino[1], Mami Matsumoto[1,5], Hisashi Oishi[6], Hiroyuki Inada[7], Yuri Ishido[1], Yukina Sakakibara[1], Huy Bang Nguyen[5,8], Truc Quynh Thai[5,9], Shinichi Kohsaka[10], Nobuhiko Ohno[11,12], Maki K. Yamada[13], Masato Asai[4], Masahiro Sokabe[14], Junichi Nabekura[7], Kenichi Asano[15], Masato Tanaka[15], and Kazunobu Sawamoto[1,2]

New neurons, continuously added in the adult olfactory bulb (OB) and hippocampus, are involved in information processing in neural circuits. Here, we show that synaptic pruning of adult-born neurons by microglia depends on phosphatidylserine (PS), whose exposure on dendritic spines is inversely correlated with their input activity. To study the role of PS in spine pruning by microglia in vivo, we developed an inducible transgenic mouse line, in which the exposed PS is masked by a dominant-negative form of milk fat globule-EGF-factor 8 (MFG-E8), MFG-E8^{D89E}. In this transgenic mouse, the spine pruning of adult-born neurons by microglia is impaired in the OB and hippocampus. Furthermore, the electrophysiological properties of these adult-born neurons are altered in MFG-E8^{D89E} mice. These data suggest that PS is involved in the microglial spine pruning and the functional maturation of adult-born neurons. The MFG-E8^{D89E}–based genetic approach shown in this study has broad applications for understanding the biology of PS-mediated phagocytosis in vivo.

Introduction

Adult mammalian brains have a remarkable capacity to generate new functional neurons. Neural stem cells (NSCs) in the adult ventricular-subventricular zone (V-SVZ) of the lateral ventricles and the subgranular zone (SGZ) of the hippocampal dentate gyrus (DG) continuously generate new neurons, which are integrated into the olfactory bulb (OB) and hippocampal circuits, respectively (Lim and Alvarez-Buylla, 2016; Song et al., 2016; Lepousez et al., 2015). In the OB, new neurons differentiate into two types of olfactory interneurons, granule cells in the granule cell layer (GCL) and periglomerular cells in the glomerular layer (GL), which form dendrodendritic synapses with mitral/tufted (M/T) cells, projection neurons in the OB, and receive centrifugal inputs from higher olfactory centers (Shepherd et al., 2004). In the DG, new neurons differentiate into granule cells in the GCL and receive neuronal inputs from the entorhinal cortex in the molecular layer (ML; Johnston and Amaral, 2004). Blocking or activating new neurons' synaptic transmission alters olfaction and memory (Hardy et al., 2018; Gao et al., 2018; Muthusamy et al., 2017; Sakamoto et al., 2014), indicating that synapses formed on new neurons are crucial for these brain functions. Recent accumulating pieces of evidence revealed various molecular mechanisms for the synapse formation of adult-born neurons (Breton-Provencher et al., 2016; Duan et al., 2014; Burk et al., 2012; Sultan et al., 2015; Tran et al., 2009). However, how synaptic pruning, another critical step for the functional integration of new neurons into circuits, is controlled in adult-born neurons is not fully understood.

Microglia, the professional phagocytes in the central nervous system, contribute to various facets of adult neurogenesis (Rodríguez-Iglesias et al., 2019; Sierra et al., 2013). Dead cells in

[1]Department of Developmental and Regenerative Neurobiology, Institute of Brain Science, Nagoya City University Graduate School of Medical Sciences, Nagoya, Japan; [2]Division of Neural Development and Regeneration, National Institute for Physiological Sciences, Okazaki, Japan; [3]Department of Genetics, Hyogo College of Medicine, Nishinomiya, Japan; [4]Department of Disease Model, Institute for Developmental Research, Aichi Developmental Disability Center, Kasugai, Japan; [5]Section of Electron Microscopy, Supportive Center for Brain Research, National Institute for Physiological Sciences, Okazaki, Japan; [6]Department of Comparative and Experimental Medicine, Nagoya City University Graduate School of Medical Sciences, Nagoya, Japan; [7]Division of Homeostatic Development, National Institute for Physiological Sciences, Okazaki, Japan; [8]Department of Anatomy, Faculty of Medicine, University of Medicine and Pharmacy at Ho Chi Minh City, Ho Chi Minh City, Vietnam; [9]Department of Histology-Embryology-Genetics, Faculty of Basic Medical Sciences, Pham Ngoc Thach University of Medicine, Ho Chi Minh City, Vietnam; [10]National Institute of Neuroscience, National Center of Neurology and Psychiatry, Kodaira, Japan; [11]Department of Anatomy, Division of Histology and Cell Biology, Jichi Medical University, School of Medicine, Shimotsuke, Japan; [12]Division of Ultrastructural Research, National Institute for Physiological Sciences, Okazaki, Japan; [13]Department of Neuropharmacology, Kagawa School of Pharmaceutical Sciences and Institute of Neuroscience, Tokushima Bunri University, Sanuki, Japan; [14]Mechanobiology Laboratory, Nagoya University Graduate School of Medicine, Nagoya, Japan; [15]Laboratory of Immune Regulation, Tokyo University of Pharmacy and Life Sciences, Hachioji, Japan.

Correspondence to Kazunobu Sawamoto: sawamoto@med.nagoya-cu.ac.jp.

the adult neurogenic regions are rapidly eliminated by microglial phagocytosis (Sierra et al., 2010; Diaz-Aparicio et al., 2020; Denizet et al., 2017). Moreover, microglia secrete and receive cytokines to promote adult neurogenesis (Diaz-Aparicio et al., 2020; Shigemoto-Mogami et al., 2014; Mosher et al., 2012; Ribeiro Xavier et al., 2015; Matsuda et al., 2015). Spine density in adult-born neurons is altered by chemical depletion of microglia in the OB and DG (Reshef et al., 2017; Wallace et al., 2020; Wang et al., 2020), suggesting a role of microglia in the synaptic dynamics of adult-born neurons. In the hippocampus, microglia phagocytose CA3 synapses of granule cells during postnatal development (Andoh et al., 2019) and dendritic spines of engram cells in the adult stage (Wang et al., 2020). Furthermore, microglia also phagocytose perisynaptic extracellular matrix to promote synaptic plasticity in adult-born neurons in the DG (Nguyen et al., 2020). However, the molecular mechanisms that control synaptic pruning by microglia in adult-born neurons in the OB and DG have been largely unknown.

Phosphatidylserine (PS) is an important membrane phospholipid that serves as an eat-me signal for phagocytes to engulf dead cells (Lemke, 2019; Segawa and Nagata, 2015; Nagata and Segawa, 2021). While PS is localized at the inner cellular membrane in live cells, it becomes exposed on the outer cellular membrane of apoptotic or damaged cells by caspase- and calcium-induced inactivation of flippases and activation of scramblases (Segawa et al., 2016, 2014; Suzuki et al., 2016, 2013). In the central nervous system, the mechanisms for PS recognition, including those mediated by milk fat globule-epidermal growth factor-factor 8 (MFG-E8)-αvβ3 integrin (Fricker et al., 2012; Fuller and Van Eldik, 2008; Neher et al., 2013), protein S/Gas6-Tyro3/Axl/Mer (TAM receptors; Fourgeaud et al., 2016; Diaz-Aparicio et al., 2020; Park et al., 2021), and triggering receptor expressed on myeloid cells 2 (TREM2; Filipello et al., 2018; Wang et al., 2015), enable microglia to efficiently identify, phagocytose, and remove cells and synapses. Recent studies reported that synapses present PS and are phagocytosed by microglia during postnatal brain development (Scott-Hewitt et al., 2020; Li et al., 2020; Park et al., 2021). Furthermore, microglial Mer and GPR56 regulate PS-mediated synaptic pruning during the postnatal stage (Li et al., 2020; Park et al., 2021), suggesting that PS acts as a synaptic eat-me signal in vivo. However, the function of PS in synaptic pruning by microglia in adult-born neurons has not been demonstrated. In addition to microglia-specific deficient mice for PS recognition molecules, tools for target-cell–specific PS blocking without affecting microglia will be also beneficial for a better understanding of the PS-mediated biological processes.

In the present study, we show that PS is localized at the dendritic spines of adult-born neurons and is involved in their pruning by microglia in the OB and DG. To investigate the role of PS in spine pruning by microglia in vivo, we generated a transgenic mouse line, in which exposed PS is masked specifically in adult-born neurons by MFG-E8^{D89E}, a dominant-negative form of the opsonin MFG-E8 (Hanayama et al., 2002; Asano et al., 2004). We found that MFG-E8^{D89E} inhibits microglial phagocytosis of spines, leading to altered spine dynamics and density, and modified electrophysiological properties in adult-born neurons.

Results

Microglia phagocytose a subset of granule cell spines in the adult OB

To study whether microglia phagocytose granule cell spines in adult OB, we performed sequential image acquisition of targeted microglia using a serial block-face scanning electron microscope (SBF-SEM; Matsumoto et al., 2019; Sawada et al., 2018; Fig. 1 [n = 23 cells from three mice] and Fig. S1 [n = 22 cells from three mice]). OB microglia were identified in SBF-SEM images based on their ultrastructural features: irregular contour with elongated processes, dark cytosol containing long endoplasmic reticulum and lysosomes, and association with extracellular space (Matsumoto et al., 2019; Fig. S1 A). While apical dendrites of granule cells form dendrodendritic synapses with secondary dendrites of M/T cells in the external plexiform layer (EPL), distal, proximal, and basal dendrites in the GCL form synapses to receive inputs from the axonal terminals of M/T cells in the OB and projection neurons in higher olfactory centers (Shepherd et al., 2004). In the SBF-SEM images, we observed dendrodendritic synapses between secondary dendrites of M/T cells and dendritic spines of granule cells in the EPL (Fig. S1 G). At these synapses, granule cell spines contained 40 nm synaptic vesicles and postsynaptic densities, as described previously (Price and Powell, 1970; Fig. S1 G). Similar 40 nm vesicles were observed in double-membrane inclusion bodies within the microglial processes (Fig. 1, A–F and J; Schafer et al., 2012). These inclusion bodies were occasionally making contact with the inner surface of the plasma membrane of microglial processes associated with a granule cell dendrite (Fig. 1, A–C and J; and Video 1; 21 events from 12 cells), suggesting that they had been engulfed immediately before fixation. The remaining inclusion bodies were detached from the microglial plasma membrane (Fig. 1, D–F and J; 59 events from 17 cells), indicating the later stage of microglial phagocytosis. Quantification analysis revealed that 50.8 ± 7.9% and 77.2 ± 10.1% of microglia showed early and later stages of spine phagocytosis, respectively (n = 3 mice). We also observed granule cell spines partially phagocytosed by microglia (Fig. 1, G–J; and Video 2; nine events from six cells [n = 3 mice]). Taken together, these results suggest that microglia phagocytose granule cell spines in the adult OB.

PS at spines is masked in MFG-E8^{D89E} transgenic mice

While recent studies reported that synapses present PS and are phagocytosed by microglia during postnatal brain development (Scott-Hewitt et al., 2020; Li et al., 2020), the synaptic localization and function of PS in synaptic pruning in adult-born neurons are still unknown. To address these points, we generated a transgenic mouse line that inhibits PS-dependent phagocytosis by using MFG-E8 mutant proteins (Fig. 2, A and B). MFG-E8 is a secreted glycoprotein that simultaneously binds to PS on targeted cells and αvβ3 integrin on phagocytes, via its C-terminal domain and arginine–glycine–aspartate (RGD) motif, respectively (Hanayama et al., 2002). A dominant negative form

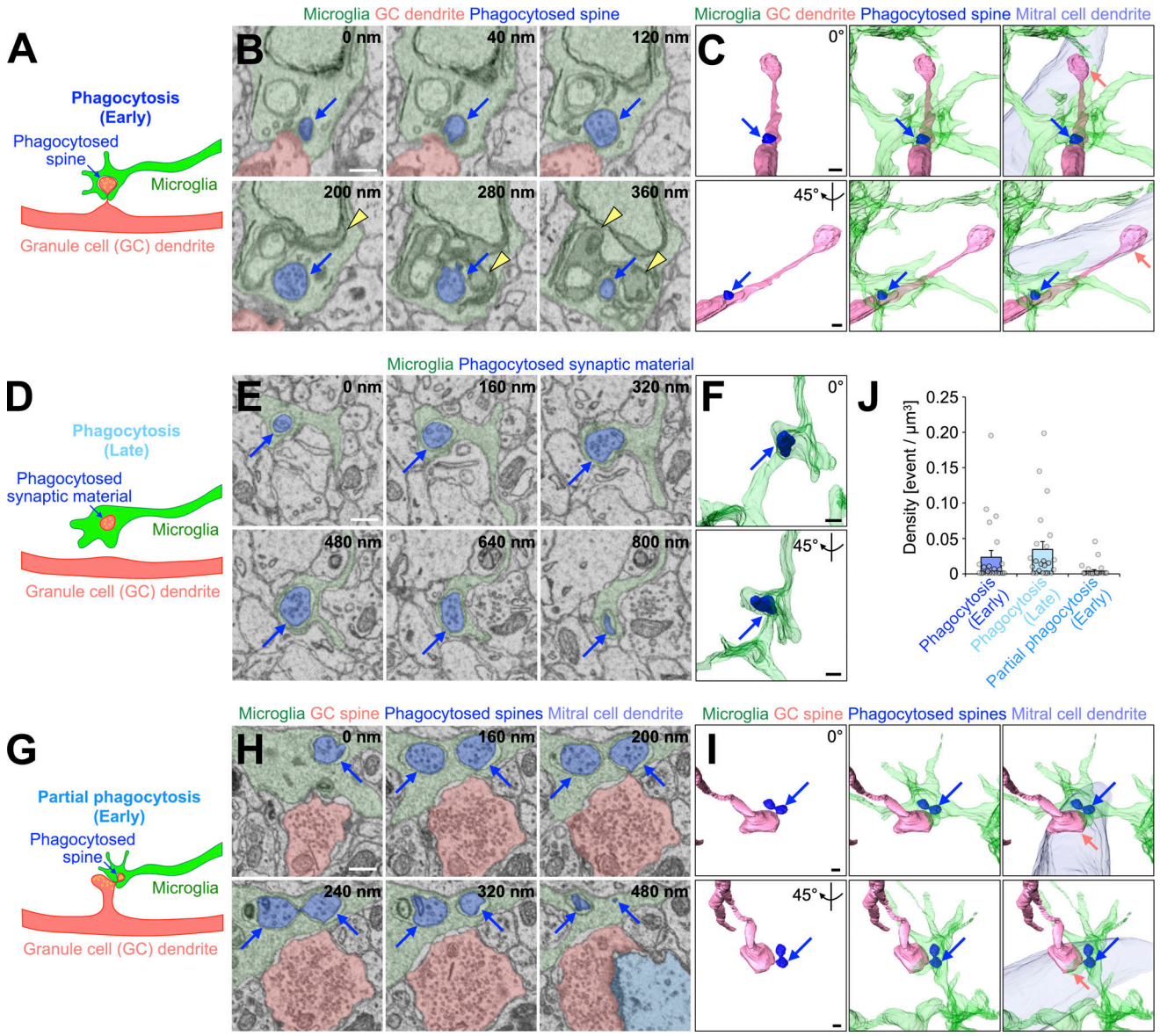

Figure 1. **Microglia phagocytose a subset of granule cell spines in the adult OB. (A–I)** Representative illustrations (A, D, and G), SBF-SEM images (B, E, and H), and 3D reconstructions (C, F, and I) of microglia (n = 23 cells from three mice, pooled from eight independent experiments) in the process of "phagocytosis (early)" (A–C), "phagocytosis (late)" (D–F), or "partial phagocytosis (early)" (G–I). Blue arrows (A–I) indicate phagocytosed spines (A–C and G–I) or synaptic material (D–F). Yellow arrowheads (B) and circles (A, D, and G) indicate lysosomes and synaptic vesicles, respectively. Microglia (A–I, green), granule cells (A–C and G–I, pink), phagocytosed spine/synaptic material (B, C, E, F, H, and I, blue), and mitral cells (C, H, and I, light blue) are also shown. Pink arrows (C and I) indicate dendrodendritic synapses between granule cell spines and mitral cell dendrites. Interactive 3D models of microglial phagocytosis shown in A–C and G–I are shown at https://sketchfab.com/3d-models/phagocytosis-of-spine-by-microglia-7f168d4801e1444fb1f14750bbad7175 and https://sketchfab.com/3d-models/partial-phagocytosis-of-spine-by-microglia-b3b4332f1bc74dea86ae81965a3d23d3, respectively. **(J)** Event per microglial volume (density) of phagocytosis (early), phagocytosis (late), or partial phagocytosis (early) (n = 23 cells from three mice, pooled from eight independent experiments). Each dot indicates data from one cell. Scale bars in B, C, E, F, H, and I, 400 nm. Data shown are mean ± SEM.

of MFG-E8, MFG-E8^{D89E}, can bind to PS but not αvβ3 integrin due to a point mutation (D89E) in the RGD motif, thereby inhibiting PS-dependent phagocytosis (Hanayama et al., 2002; Asano et al., 2004; Fig. 2 B, right). As a control, we used a deletion mutant lacking the C-terminal domain, MFG-E8^{EPT}, which does not mask PS (Hanayama et al., 2002; Asano et al., 2004; Fig. 2 B, left). To induce the secretion of MFG-E8^{EPT} or MFG-E8^{D89E} protein from adult-born neurons, *Dcx-CreER^{T2}; R26-tdTomato* mice (Fujioka et al., 2017) were crossed with *R26-MFG-E8$^{EPT\ or\ D89E}$* (*R26-EPT* or *D89E*) mice to generate *Dcx-CreER^{T2}; R26-EPT or D89E; R26-tdTomato* mice (hereafter referred to as *EPT* or *D89E* mice). In these lines, tamoxifen injection at the adult stage induced the Cre-mediated recombination and subsequent expression of tdTomato and MFG-E8$^{EPT\ or\ D89E}$ in Dcx-expressing cells but not in GFAP-expressing astrocytes or Iba1-expressing microglia (Fig. 2, A and B; and Fig. S2, A and B).

To detect synaptic PS in the adult OB, we injected a PSVue probe, which labels PS exposed on the outer surface of the

JEM

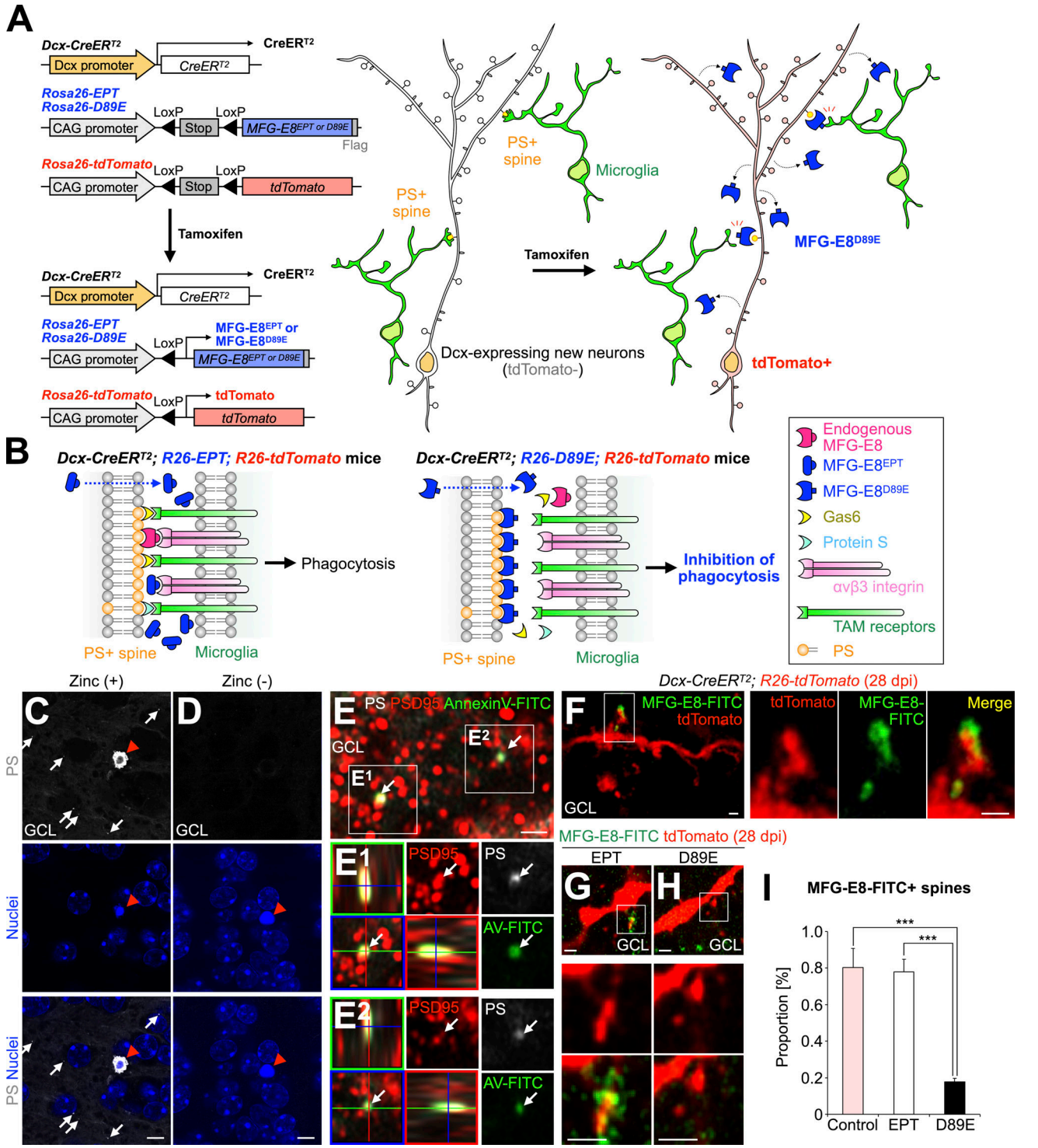

Figure 2. **MFG-E8^{D89E} masks PS exposed at spines in vivo. (A)** Schematic illustration of the transgenic mouse lines developed in the study. Left: Following Cre-mediated excision of the LoxP-flanked "Stop" sequence, MFG-E8^{EPT} and MFG-E8^{D89E} (see explanation in B) are expressed under the control of the *CAG* promoter located in the *Rosa26* locus. *Dcx-CreER^{T2}* mice were used for Tamoxifen-induced recombination in Dcx-expressing new neurons in the adult brain. *Rosa26-tdTomato* mice were used to visualize recombined Dcx-expressing cells. Right: Tamoxifen-induced expression of MFG-E8^{D89E} in Dcx-expressing cells in the adult brain. MFG-E8^{D89E} (blue) is specifically secreted from Dcx-expressing new neurons and masks PS^{+} spines (yellow) to suppress microglial phagocytosis. Recombined new neurons are visualized by tdTomato expression (red). **(B)** Mechanism for the inhibition of PS-dependent phagocytosis by MFG-E8^{D89E}. Under physiological conditions, PS on damaged or apoptotic cells/synapses is recognized by adaptor molecules from several phagocytic pathways, including the MFG-E8-αvβ3 integrin pathway (magenta and pink, respectively) and the Protein S/Gas6/TAM receptors pathway (light blue, yellow, and green, respectively). Overexpressed MFG-E8^{EPT} (left, blue), which binds to αvβ3 integrin but not PS, does not interfere with phagocytosis. On the contrary, overexpressed MFG-E8^{D89E} (right, blue), which is a dominant-negative form of MFG-E8, binds to PS but not αvβ3 integrin, hindering PS recognition and subsequent phagocytosis. **(C and D)** Representative images of the GCL in the OB of adult WT mice injected with PSVue550 (white) with (C) or without (D) zinc solution (*n* =

3 mice). White arrows and red arrowheads indicate PS+ dots and a pyknotic cell, respectively. Nuclei are stained by Hoechst 33342 (blue). **(E)** Representative images of the GCL in the OB of adult WT mice injected with PSVue550 (white) and AnnexinV-FITC (green), stained for postsynaptic marker PSD95 (red; *n* = 3 mice, pooled from two independent experiments). The boxed area is enlarged in the bottom. Arrows in the boxed area (E^1 and E^2, orthogonal view) indicate PS+AnnexinV-FITC+PSD95+ signal. **(F–H)** Representative images of the GCL in the OB of control (F, *n* = 3 mice), *EPT* (G, *n* = 3 mice), and *D89E* (H, *n* = 4 mice) mice injected with MFG-E8-FITC (green). The boxed areas (F–H) are enlarged in the right (F) and bottom (G and H). **(I)** Proportion of MFG-E8-FITC+tdTomato+ spines in control (*n* = 3 mice), *EPT* (*n* = 3 mice), and *D89E* (*n* = 4 mice) mice (pooled from three independent experiments; $F_{(2,7)}$ = 33.2, P = 0.00027, one-way ANOVA; control versus *D89E*, P = 0.00053, *EPT* versus *D89E*, P = 0.00067, Tukey–Kramer test). GCL, granule cell layer. Scale bars in C and D, 5 µm; E–H, 1 µm. ***, P < 0.005. Data shown are mean ± SEM.

cellular membrane (Scott-Hewitt et al., 2020; Li et al., 2020) into the OB. The PSVue signals were observed as small dots in non-pyknotic cells in addition to pyknotic cells in the GCL in a zinc-dependent manner, as reported previously (Scott-Hewitt et al., 2020; Li et al., 2020; Fig. 2, C and D). To determine whether PS is localized to synaptic structures, we injected PSVue550 and AnnexinV-FITC, which also labeled exposed PS (Koopman et al., 1994), and performed immunostaining for the postsynaptic marker PSD95. PSVue550 was colocalized with AnnexinV-FITC at PSD95+ spines (Fig. 2 E; 94.1 ± 3.0% [*n* = 3 mice]), suggesting that post-synapses present PS in the adult OB. Similar PSVue signals were observed at spines even in the postfixed OB sections (Fig. S3, A–C). Furthermore, the exposed PS signals were not detectable in the cell body of adult-born neurons (Fig. S3, E–G), suggesting that synaptic PS exposure is not attributable to apoptosis. Taken together, these results suggest that post-synapses present PS in the adult OB.

We next studied the distribution of MFG-E8-FITC injected into the OB of control (*Dcx-CreER^{T2}; R26-tdTomato*), *EPT*, and *D89E* mice at 28 d post-tamoxifen injection (dpi). The MFG-E8-FITC signals were associated with spines of tdTomato+ granule cells in control mice (Fig. 2 F), suggesting that MFG-E8 is localized at the spines of adult-born neurons. Moreover, binding of MFG-E8-FITC to tdTomato+ spines was inhibited in *D89E* but not *EPT* mice (Fig. 2, G–I), suggesting that MFG-E8^{D89E} competes with MFG-E8-FITC for their binding to spines. These results suggest that MFG-E8^{D89E} specifically masks PS exposed on the spines of adult-born neurons.

PS exposure is involved in microglial phagocytosis of spines of adult-born neurons in the OB

To evaluate the activity level of PS+ synapses, we used the F-actin capping protein CapZ, which is accumulated in spines given high-frequency inputs (Kitanishi et al., 2010). In *AiCE-Tg* transgenic mice (Kuboyama et al., 2020), expressing EGFP-tagged CapZ protein, the intensity of EGFP fluorescence in spines reflects both the level of received inputs to spines and cellular activity (*Arc* promoter-dependent expression). We occluded the left naris of *AiCE-Tg* mice and here defined active spines as PSD95+ spines with higher EGFP intensity than those with mean of EGFP signals in the highest 100 spines in naris-occluded side of OBs (Fig. 3, D–G; see Materials and methods). Odor-input deprivation was confirmed by the decrease in the density of c-Fos+ cells in the GCL in the occluded side (Fig. 3, A–C). These EGFP+PSD95+ spines contained Bassoon, a component of the active zone (Whitman and Greer, 2007; Fig. 3 F). PS signal was never observed in the active spines but was found in a small but significant subset of other spines (0.63%; Fig. 3 G). Taken together, these results suggest that PS preferentially labels spines that receive lower neuronal inputs.

To support this idea, we further investigated whether PS exposure on spines was affected by olfactory input and tested the effects of 2-d odor deprivation or enrichment in adult WT mice (Sawada et al., 2011; Kato et al., 2012). The density of PSD95+PS+ spines was significantly increased and decreased by odor deprivation and enrichment, respectively (Fig. 3, H–K), indicating that the PS exposure is inversely correlated with the input activity of spines in the adult OB.

To examine the role of PS in microglia–synapse interaction, we compared microglial contacts to spines of tdTomato+ granule cells in *EPT* and *D89E* mice at 28 dpi. Microglial contacts with spines were classified into three categories based on the area of the spine surface covered by the microglial process: touching, spreading, and wrapping (Fig. 4 A; see Materials and methods). This microglia–spine interaction was also confirmed in SBF-SEM analyses (Fig. S1, A–E). Spiny protrusions were morphologically classified into filopodia, thin, stubby, and mushroom types (Breton-Provencher et al., 2014; Fig. S4 A). The proportion of spines expressing PSD95 was lower in the thin type than in stubby and mushroom types (Huang et al., 2015), suggesting that the thin-type spines are immature. We found that 62.4 ± 2.6% of spreading microglial processes (*n* = 3 mice) and 71.4 ± 4.8% of wrapping microglial processes (*n* = 3 mice) were making contact with thin-type spines, indicating that microglia preferentially wrap immature spines (Fig. S4, B and C). The densities of microglial touching to, spreading on, and wrapping of tdTomato+ spines were not significantly different between control and *EPT* mice (Fig. 4, B and D–F), suggesting that MFG-E8^{EPT} overexpression does not affect microglia–synapse interaction. Interestingly, the densities of microglial spreading on and wrapping of but not touching to the spines in *D89E* mice were significantly lower than those in *EPT* mice (Fig. 4, C–F). These results demonstrate that microglial spreading and wrapping of spines depend on PS exposure.

To investigate whether microglial phagocytosis of spines is also inhibited in *D89E* mice, we stained OB sections for Iba1, PSD95, and CD68, a marker for lysosomes, in control, *EPT*, and *D89E* mice at 28 dpi. The density of PSD95+tdTomato+ spines within the CD68+ lysosomes in Iba1+ microglial processes was significantly decreased in *D89E* but not *EPT* mice (Fig. 4, G and H; and Video 3), suggesting that the microglial phagocytosis of spines was suppressed. Consistently, the proportion of PS+ spines was significantly increased in *D89E* mice (Fig. S2, C–E). MFG-E8^{EPT} and MFG-E8^{D89E} did not affect the migration of tdTomato+ adult-born neurons into the OB or the number of Iba1+ microglia in the OB (Fig. S2, F–J). Taken together, these

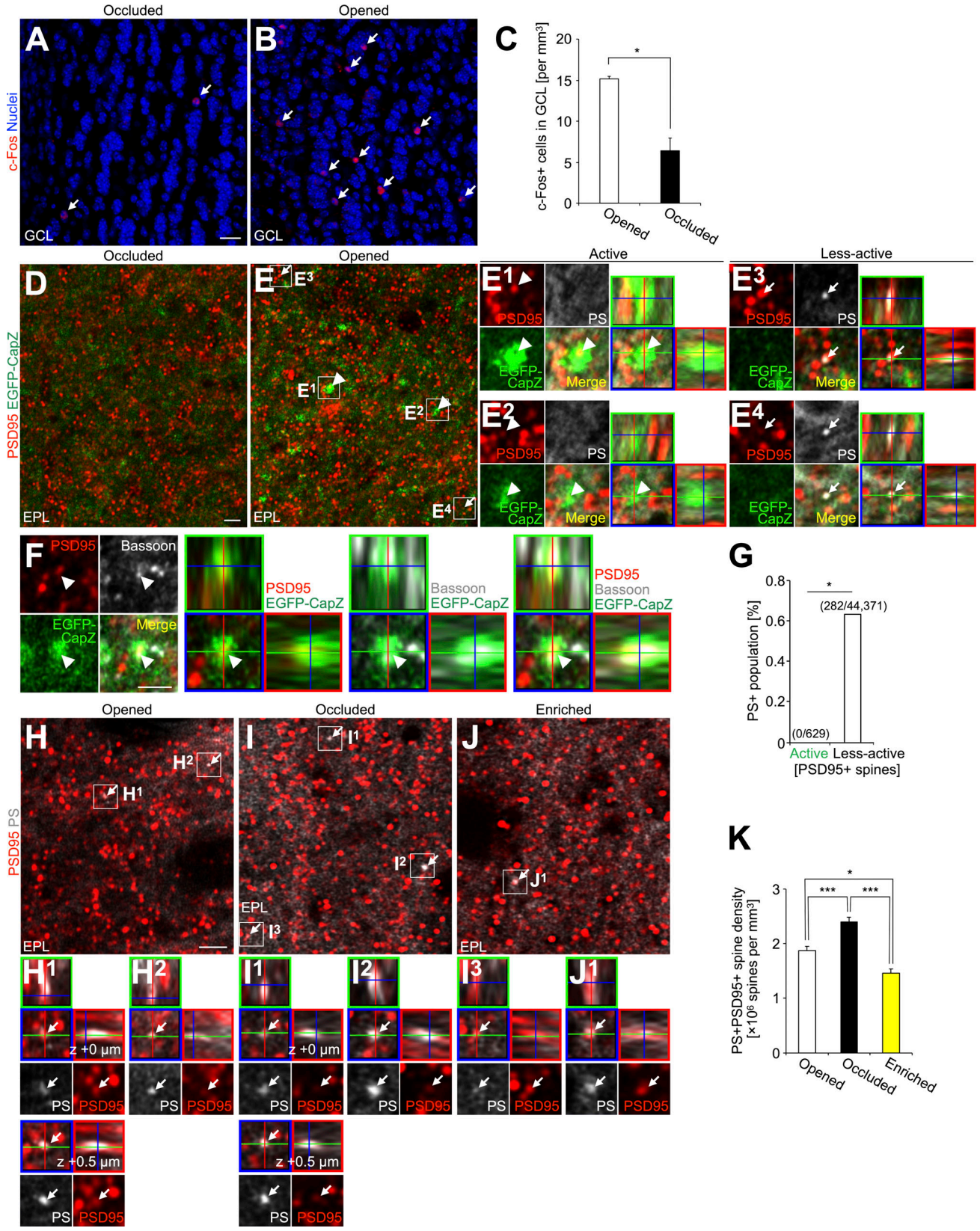

Figure 3. **PS exposure on less-active spines, and its suppression by olfactory inputs in the adult OB. (A and B)** Representative images c-Fos staining (red) of the GCL in the naris-occluded (A) and opened (B) side of OB in adult *AiCE-Tg* mice (n = 3 mice) with unilateral naris occlusion. Nuclei were stained with Hoechst 33342 (blue). Arrows indicate c-Fos$^+$ signals in the GCL. **(C)** Density of the c-Fos$^+$ cells in the GCL (n = 3 mice, pooled from two independent experiments, $t_{(2)} = -7.7$, P = 0.016, paired t test). **(D and E)** Representative images of the EPL in the naris-occluded (D) and opened (E) side of OB in the adult *AiCE-Tg* mice (n = 3 mice) stained for PS (white), PSD95 to define spines (red), and EGFP (green, EGFP-CapZ). Active and less-active spines, defined here by the level

of EGFP signal (see Materials and Methods), in E are enlarged and shown by orthogonal view in (E^1 and E^2) and (E^3 and E^4), respectively. Arrowheads and arrows (E and E^1–E^4) indicate active spines and representative PS^+ spines, respectively. **(F)** Representative single z-plane and orthogonal images of the active spine (arrowhead) in the EPL of the naris-opened side of the OB of adult *AiCE-Tg* mice (n = 3 mice) stained for the postsynaptic marker PSD95 (red), EGFP (green, EGFP-CapZ), and a presynaptic marker Bassoon (white). **(G)** Proportion of PS^+ population in active and less-active $PSD95^+$ spines in the EPL of the adult OB (pooled from two independent experiments; 0 PS^+/629 active spines, 282 PS^+/44,371 less-active spines from two mice; P = 0.037, Fisher's exact test). **(H–J)** Representative images of the EPL in the OB of naris-opened (H, n = 4 mice), naris-occluded (I, n = 4 mice), and odor-enriched (J, n = 6 mice) adult WT mice stained for PS (white) and PSD95 (red). $PSD95^+PS^+$ spines (arrows) are enlarged and shown by orthogonal view in the boxes (H^1, H^2, I^1, I^2, I^3, and J^1). Different z-level images of $PSD95^+PS^+$ spine in (H^1 and I^1) are also shown by a single z-plane and orthogonal view (z + 0.5 µm). **(K)** Density of the $PSD95^+PS^+$ spines (n = 4 [opened], 4 [occluded], 6 [odor-enriched] mice pooled from two independent experiments; $F_{(2,11)}$ = 33.3, P = 0.000022, one-way ANOVA; opened versus occluded, P = 0.0041, opened versus enriched, P = 0.011, occluded versus enriched, P = 0.000015, Tukey–Kramer test). GCL, granule cell layer; EPL, external plexiform layer. Scale bars: A, B, 20 µm; D–F and H–J, 2 µm. *, P < 0.05; ***, P < 0.005. Data shown are mean ± SEM.

results suggest that PS is involved in the phagocytosis of immature spines by microglia in adult-born neurons in the OB.

To examine the effects of olfactory input on the microglia–spine interaction, we analyzed microglial contacts and phagocytosis of spines in naris-occluded *EPT* and *D89E* mice at 28 dpi. Consistent with the enhanced PS exposure on the spines of naris-occluded WT mice (Fig. 3, H–K), the three-day naris occlusion significantly increased the densities of microglial spreading and wrapping of $tdTomato^+$ spines (Fig. 4, D–F) and the density of $PSD95^+tdTomato^+$ spines incorporated in the $CD68^+$ lysosomes in $Iba1^+$ processes (Fig. 4 H) in *EPT* but not *D89E* mice. These results support that PS exposure on spines, inversely correlated with sensory input activity, is coupled with microglial spreading, wrapping, and subsequent phagocytosis of spines of adult-born neurons in the OB.

To study the dynamics of microglial phagocytosis of spines of adult-born neurons and the involvement of PS in these processes in live animals, we performed in vivo two-photon time-lapse imaging of microglia and adult-born neurons in *EPT* or *D89E; Iba1-EGFP* mice (Fig. 5 A; and Fig. S5, A and B). Consistent with histological analyses (Fig. 4), $EGFP^+$ microglial processes touched and wrapped $tdTomato^+$ spines in *EPT; Iba1-EGFP* mice (Fig. 5, B–D; and Video 4). While most of the microglial touching and wrapping of spines were transient, these microglial contacts occasionally proceeded to phagocytosis of spines in *EPT; Iba1-EGFP* mice (Fig. 5, B–E; and Video 4). Following phagocytosis, $tdTomato^+$ debris were observed in $EGFP^+$ microglial processes (Fig. 5, B and E, arrowheads). These results suggest that the microglial touching, wrapping of, and phagocytosis of spines are sequential steps in the adult OB. In *D89E; Iba1-EGFP* mice, the frequency of microglial wrapping and phagocytosis, but not touching, of $tdTomato^+$ spines, was significantly decreased (Fig. 5, F and G; and Video 5). Taken together, these results suggest that PS is involved in the microglial membrane extension along targeted spines of adult-born neurons in the OB.

PS is involved in the dendritic spine pruning of adult-born neurons in the OB

To investigate the effect of $MFG\text{-}E8^{D89E}$ on adult-born neurons' spine dynamics in the OB, we performed in vivo two-photon imaging of dendritic spines of $tdTomato^+$ granule and periglomerular cells at 28 and 30 dpi in *EPT* and *D89E* mice (Fig. 6 and Fig. S5, C–H). By comparing two consecutive images captured at 2-d interval, the spines were classified as added, lost, and stable (Sailor et al., 2016; Fig. 6 A). The percentages of added and lost spines of granule cells were not significantly different in adult *EPT* mice (Fig. 6, B and D), as was reported previously in adult WT mice (Sailor et al., 2016). In contrast, the percentage of lost spines was significantly lower than that of added spines in *D89E* mice (Fig. 6, C and D). Furthermore, we also noted that the proportion of lost spines in *D89E* mice was significantly lower than that in *EPT* mice (Fig. 6 D). A similar decrease in spine pruning was also observed in periglomerular cells in *D89E* mice (Fig. 6, E–G). Together, these results show that PS affects the spine dynamics of adult-born neurons in the OB.

The decrease in the lost population of spines (Fig. 6, D and G) of adult-born neurons in *D89E* mice could be attributable to (1) failure of spine pruning and/or (2) promotion of filopodium formation and suppression of filopodium retraction. To address these possibilities, we performed in vivo two-photon time-lapse imaging of filopodium dynamics in granule cells and found no effect of $MFG\text{-}E8^{D89E}$ on filopodium formation and retraction (Fig. S5, E–H). Thus, our results support the idea that PS is involved in the spine pruning of adult-born neurons in the OB.

Inhibition of PS-dependent spine pruning by $MFG\text{-}E8^{D89E}$ increases the spine density in adult-born mature neurons in the OB

In granule cells of the adult OB, the spine density reaches its peak 4 wk after cell generation in the V-SVZ, and subsequently decreases during the following 4-wk-long functional development of neuronal connections (Whitman and Greer, 2007). To examine whether PS-mediated spine pruning (Figs. 2, 3, 4, 5, and 6) affects spine density in adult-born neurons, we compared the density of total spiny protrusions in granule and periglomerular cells at 28 and 56 dpi in control, *EPT*, and *D89E* mice (Fig. 7 A). Spine density in granule and periglomerular cells in these three mouse lines showed no significant difference at 28 dpi (Fig. 7 B), suggesting that synaptogenesis is not affected by $MFG\text{-}E8^{EPT}$ or $MFG\text{-}E8^{D89E}$. In control and *EPT* mice, the density of total spiny protrusions in granule cells and periglomerular cells was decreased by spine pruning from 28 to 56 dpi (Fig. 7 B), as reported previously for WT mice (Whitman and Greer, 2007). In contrast, this spine pruning was disrupted in *D89E* mice. To examine whether the effects of *D89E* on spine pruning are region-specific, granule cell dendrites were subdivided into four regions: apical, distal, proximal (<30 µm from the soma), and basal (Lepousez et al., 2014; Fig. 7 C). Apical dendrites of granule cells receive inputs from secondary dendrites of M/T cells in the EPL. On the other hand, distal, proximal, and basal dendrites in

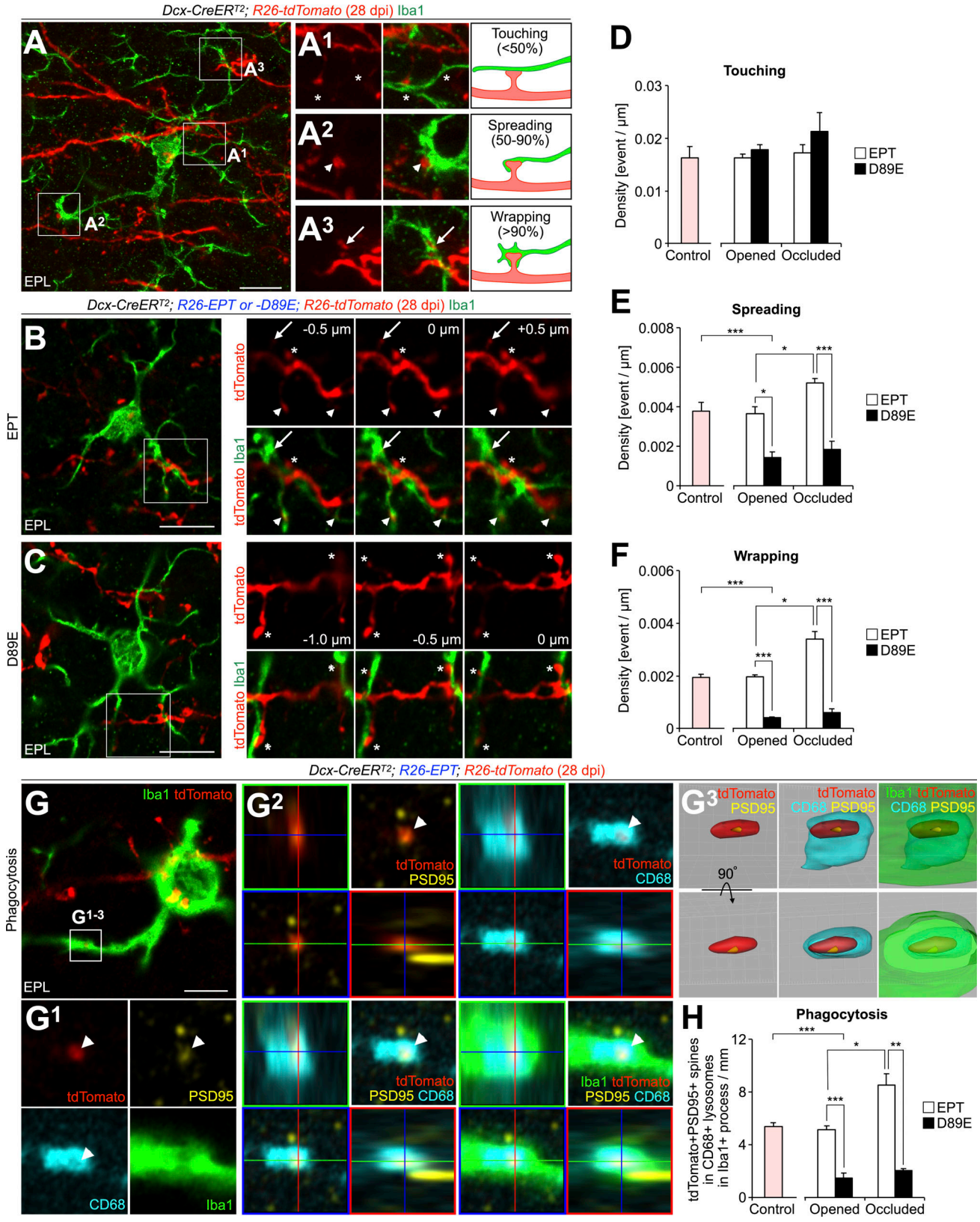

Figure 4. **PS is involved in microglial phagocytosis of spines of adult-born neurons in the OB. (A)** Representative image of the EPL in the OB of adult *Dcx-CreER^{T2}; R26-tdTomato* (control) mice at 28 dpi (n = 4 mice) stained for DsRed (red) and Iba1 (green). The boxed areas in A are enlarged in A^1–A^3. Contacts between microglia and spines are classified into three types: touching (A^1, asterisks), spreading (A^2, arrowheads), and wrapping (A^3, arrows). **(B and C)** Effect of MFG-E8^{D89E} on spine contacts by microglia in adult-born neurons in the OB. Representative images of the EPL in the OB of adult *Dcx-CreER^{T2}; R26-EPT; R26-tdTomato* (B, *EPT*, n = 5 mice), and *Dcx-CreER^{T2}; R26-D89E; R26-tdTomato* (C, *D89E*, n = 3 mice) mice at 28 dpi stained for DsRed (red) and Iba1 (green) are shown.

The boxed areas (B and C) are displayed on the right-hand side (0 µm). Asterisks, arrowheads, and arrows in the three consecutive images (B, C, right) indicate microglial touching to, spreading on, and wrapping of spines, respectively. **(D–F)** Density of microglial contacts (touching [D], spreading [E], and wrapping [F]) to spines in the adult control (n = 4 mice), naris-opened or occluded *EPT* (n = 5 mice each) or *D89E* (n = 3 mice each) mice (E, for comparison among control, *EPT*, and *D89E* mice, $F_{(2,9)}$ = 10.8, P = 0.0041, one-way ANOVA; control versus *D89E*, P = 0.0045, Dunnett's test; for comparison of *EPT* versus *D89E* and opened versus occluded, $F_{\text{mouse }(1,12)}$ = 72.6, P = 2.0 × 10^{-6}, $F_{\text{occlusion }(1,12)}$ = 8.87, P = 0.012, two-way ANOVA; *EPT* versus *D89E* in opened, $t_{(6)}$ = 4.4, P = 0.018, opened versus occluded in *EPT*, $t_{(8)}$ = −3.8, P = 0.021, *EPT* versus *D89E* in occluded, $t_{(6)}$ = 8.0, P = 0.00082, unpaired t test; F, for comparison among control, *EPT*, and *D89E* mice, $F_{(2,9)}$ = 93.6, P = 9.5 × 10^{-7}, one-way ANOVA; control versus *D89E*, P = 1.6 × 10^{-6}, Dunnett's test; for comparison of *EPT* versus *D89E* and opened versus occluded, $F_{\text{mouse }(1,12)}$ = 128, P = 9.1 × 10^{-8}, $F_{\text{occlusion }(1,12)}$ = 18.3, P = 0.0011, two-way ANOVA; *EPT* versus *D89E* in opened, $t_{(6)}$ = 15.4, P = 1.9 × 10^{-5}, opened versus occluded in *EPT*, $t_{(8)}$ = −5.2, P = 0.018, *EPT* versus *D89E* in occluded, $t_{(6)}$ = 7.6, P = 0.0011, unpaired t test). Pink bars indicate data from controlmice. Data are pooled from 10 independent experiments. **(G)** Representative images of EPL in the OB of adult *EPT* mice (n = 4 mice) stained for PSD95 (yellow), CD68 (cyan), and Iba1 (green). tdTomato$^+$ signals (red) are directly observed without staining. The boxed area in G is enlarged (G^1) and is shown by orthogonal (G^2) and a surface-rendered 3D view (G^3). White arrowheads indicate tdTomato$^+$PSD95$^+$ spine incorporated in CD68$^+$ lysosomes within Iba1$^+$ processes (G^1). Also, see Video 3. **(H)** Density of tdTomato$^+$PSD95$^+$ spines incorporated in CD68$^+$ lysosomes within Iba1$^+$ processes in the adult control (n = 3 mice), naris-opened or occluded *EPT* (n = 4 [opened] or 3 [occluded] mice) or *D89E* (n = 3 mice each) mice (for comparison among control, *EPT*, and *D89E* mice, $F_{(2,7)}$ = 41.0, P = 0.00014, one-way ANOVA; control versus *D89E*, P = 0.00018, Dunnett's test; for comparison of *EPT* versus *D89E* and opened versus occluded, $F_{\text{mouse }(1,9)}$ = 110.7, P = 2.3 × 10^{-6}, $F_{\text{occlusion }(1,9)}$ = 16.8, P = 0.0027, $F_{\text{mouse×occlusion }(1,9)}$ = 8.8, P = 0.016, two-way ANOVA; *EPT* versus *D89E* in opened, $t_{(5)}$ = 7.6, P = 0.0025, opened versus occluded in *EPT*, $t_{(5)}$ = −4.2, P = 0.035, *EPT* versus *D89E* in occluded, $t_{(4)}$ = 7.3, P = 0.0074, unpaired t test). Pink bar indicates data from control mice. Data are pooled from six independent experiments. EPL, external plexiform layer. Scale bars: A–C, 10 µm; G, 5 µm. *, P < 0.05; **, P < 0.01; ***, P < 0.005; adjusted with Bonferroni correction. Data shown are mean ± SEM.

the GCL receive inputs from axonal terminals of M/T cells in the OB and projection neurons in higher olfactory centers (Shepherd et al., 2004). When comparing with the dendrites in *EPT* mice, we found that the density of total protrusions was significantly increased only in proximal and apical dendrites in *D89E* mice (Fig. 7, D and F). Furthermore, the density of mushroom spines was also significantly increased exclusively in the apical dendrites in *D89E* mice (Fig. 7, E and F). This regional difference in the density of total protrusion was attributable to that in the distributions of PS$^+$ spines and microglial contact (Fig. S4, E–I). Together, these results reveal that PS-mediated spine pruning controls the density of synapses in a dendritic region-specific manner in adult-born granule cells in the OB.

Inhibition of PS-dependent spine pruning by MFG-E8^{D89E} disrupts synaptic maturation of adult-born neurons in the hippocampal DG

In the hippocampal DG, adult-born neurons generated from NSCs in the SGZ develop their dendritic spines in the GCL and ML, where their density continues to increase for two months (Zhao et al., 2006). To elucidate whether PS-dependent spine pruning also occurs in adult-born neurons in the DG, we first examined PS exposure in the hippocampal synapses. Dot-like signals of injected PSVue were overlapped with those of PSD95 (Fig. 8, A and B; and Fig. S3 D), indicating the localization of PS on a subset of postsynaptic structures of granule cells in the adult ML. Furthermore, in *Dcx-CreER^{T2}; R26-tdTomato* mice, tdTomato$^+$PS$^+$ spines were wrapped by microglial processes at 28 dpi (Fig. S4 D). Interestingly, 76.9 ± 3.5% and 75.7 ± 8.4% (n = 3 mice) of spread and wrapped spines, respectively, were of the thin type, confirming that microglia preferentially wrap immature spines of adult-born neurons in the DG as well. These observations demonstrate that a subset of dendritic spines of adult-born neurons presents PS and is phagocytosed by microglia in the hippocampal DG.

To investigate the role of PS in the spine pruning of adult-born neurons in the DG, we compared microglia–spine interactions, as well as the microglial phagocytosis of spines, between *EPT* and *D89E* mice at 28 dpi. The densities of microglial spreading on and wrapping of, but not touching to spines, were significantly lower in *D89E* mice than those in *EPT* mice (Fig. 8 C). Moreover, the density of PSD95$^+$tdTomato$^+$ spines incorporated in the CD68$^+$ lysosomes in Iba1$^+$ processes was significantly decreased in *D89E* mice (Fig. 8 D and Video 6). Together, these results show that PS is involved in the microglial phagocytosis of spines of adult-born neurons in the DG.

To study the effect of MFG-E8^{D89E} on the synaptic development of adult-born neurons in the DG, we compared the densities of total protrusions and mushroom spines between *EPT* and *D89E* mice at 56 dpi, i.e., at the peak of synaptic maturity of the studied neurons (Zhao et al., 2006). There was no significant difference in the density of tdTomato$^+$NeuN$^+$ mature granule cells between *EPT* and *D89E* mice (Fig. 8, E and F), suggesting that MFG-E8^{D89E} did not affect their survival. While the density of total protrusions was increased in *D89E* mice compared with *EPT* mice (Fig. 8, G and H), the density of mushroom spines was decreased, suggesting that synaptic development is disrupted by MFG-E8^{D89E}. Taken together, these results demonstrate that PS is involved in the spine pruning of adult-born neurons by microglia in the DG.

Finally, to examine whether the observed morphological differences between spines correlated with their electrophysiological function, we measured miniature excitatory postsynaptic currents (EPSCs) in adult-born neurons in *EPT* and *D89E* mice. Whole-cell patch-clamp recordings were performed from tdTomato$^+$ adult-born neurons at 65–74 dpi in acute brain slices of *EPT* and *D89E* mice (Fig. 8 I). Adult-born neurons in *EPT* and *D89E* mice showed similar input resistance (*EPT*, 138.7 ± 15.4 MΩ, n = 8 cells; *D89E*, 147.7 ± 8.9 MΩ, n = 6 cells; P > 0.05, unpaired t test), resting membrane potentials (*EPT*, −66.3 ± 2.4 mV, n = 8 cells; *D89E*, −60.2 ± 3.9 mV, n = 6 cells; P > 0.05, unpaired t test), and the maximum number of action potentials (*EPT*, 11.4 ± 0.9, n = 8 cells; *D89E*, 10.3 ± 1.0, n = 6 cells; P > 0.05, unpaired t test), suggesting that their passive membrane properties and excitability were comparable in both groups. On the other hand, the frequency of high-amplitude events in *D89E* mice was smaller than that in *EPT* mice (Fig. 8 J, inset), suggesting a decrease in the ratio of spines with large inputs in *D89E* mice.

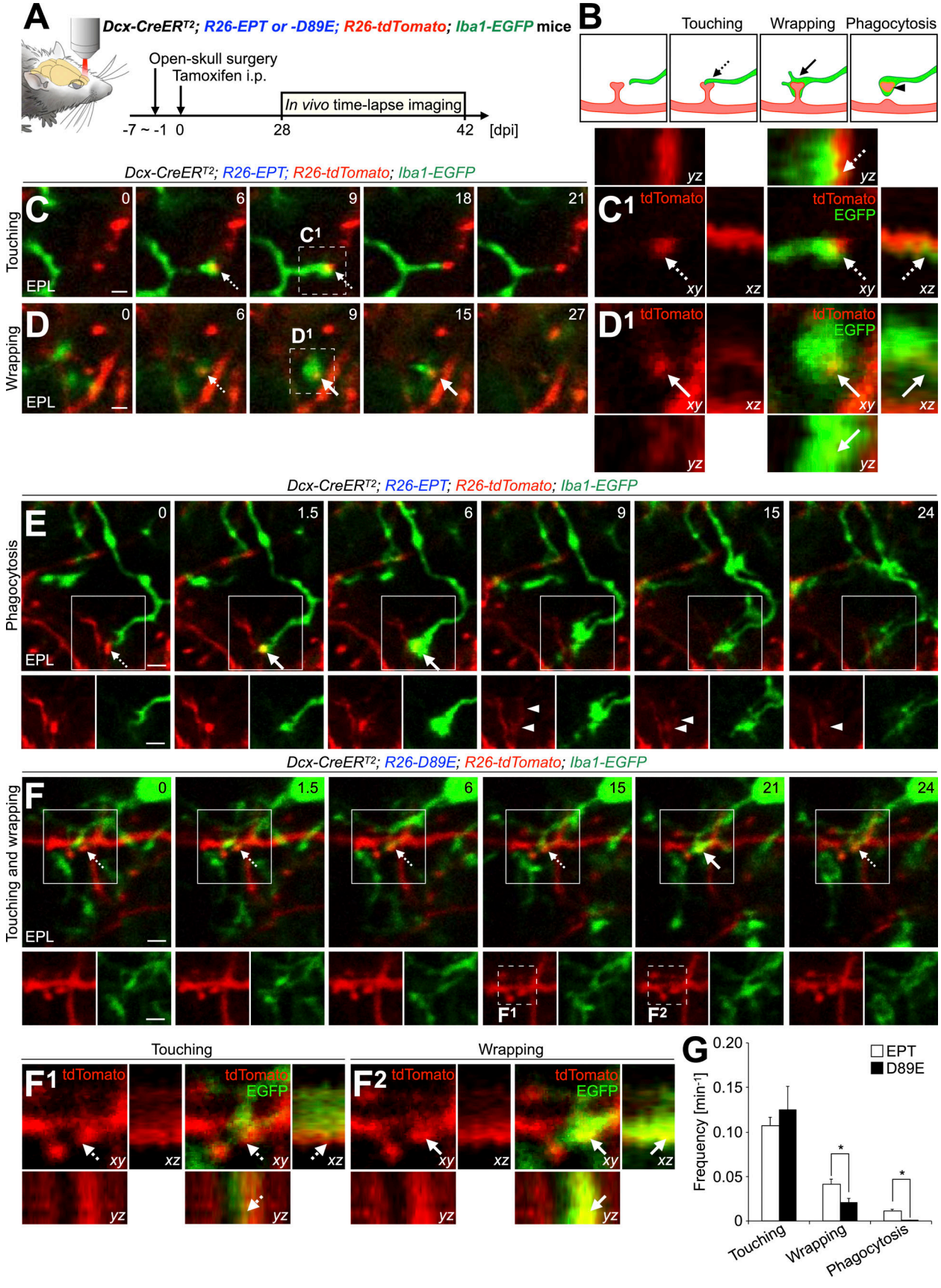

Figure 5. **PS is involved in the microglial membrane extension along targeted spines to proceed phagocytosis in adult-born neurons in the OB. (A)** Experimental scheme. In vivo two-photon imaging of dendritic spines of tdTomato$^+$ granule cells and EGFP$^+$ microglia in the adult *Dcx-CreER^{T2}; R26-EPT;*

R26-tdTomato; Iba1-EGFP (*EPT; Iba1-EGFP*) and *Dcx-CreER^{T2}; R26-D89E; R26-tdTomato; Iba1-EGFP* (*D89E; Iba1-EGFP*) mice was performed at 28–42 dpi. **(B)** Classification of microglia–spine interaction in two-photon imaging. **(C–F)** Representative two-photon images of dendrites of tdTomato$^+$ granule cells (red) and EGFP$^+$ microglial processes (green) in the adult OB of *EPT* (C–E, also see Fig. S5, A and B; and Video 4; n = 3 mice) or *D89E* (F, also see Video 5; n = 5 mice); *Iba1-EGFP* mice. Dotted line boxes in C and D are magnified and shown in orthogonal view (C^1 and D^1), respectively. Dotted line boxes (F, 15 and 21 min) are magnified and shown in orthogonal view (F^1 and F^2), respectively. **(G)** Frequency of microglial touching to, wrapping of, and phagocytosis of tdTomato$^+$ spines in *EPT or D89E; Iba1-EGFP* mice (n = 3 or 5 mice pooled from three or five independent experiments, respectively; wrapping, $t_{(6)}$ = 2.5, P = 0.047, unpaired t test; Phagocytosis, P = 0.032, Welch's t test). EPL, external plexiform layer. Dashed and solid arrows indicate microglial touching to and wrapping of spines, respectively (B–F). Arrowheads indicate phagocytosed spines observed in the microglial processes (B and E). Numbers (C–F) indicate minutes after the first imaging frame. Scale bars, 2 µm. *, P < 0.05. Data shown are mean ± SEM.

In addition, the distribution of interevent intervals in *D89E* mice was significantly shifted toward longer intervals (Fig. 8 K), suggesting a decrease in the total number of functional spines in *D89E* mice. Taken together, these results indicate that PS-dependent spine pruning by microglia contributes to the synaptic maturation of adult-born neurons in the DG.

Discussion

PS as a synaptic eat-me signal

PS is exposed on the outer plasma membrane of apoptotic cells and serves as an eat-me signal for phagocytes (Segawa and Nagata, 2015; Nagata and Segawa, 2021). A recent study suggests that degenerating dendrites of neurons also present PS and are phagocytosed by epidermal cells in *Drosophila melanogaster* (Sapar et al., 2018). In rodents, synapses present PS and are phagocytosed by microglia during postnatal brain development (Scott-Hewitt et al., 2020; Li et al., 2020; Park et al., 2021). Microglia deficient for TREM2, GPR56, and Mer, all of which directly or indirectly bind to PS, showed defects in phagocytosis of PS$^+$ liposomes (Scott-Hewitt et al., 2020) and synaptic pruning ability (Li et al., 2020; Park et al., 2021), suggesting that PS acts as an eat-me signal for microglia during brain development. Here, we developed a transgenic mouse line expressing MFG-E8^{D89E}, which specifically masks PS in vivo, and found a disrupted spine pruning by microglia in adult-born neurons in these mice. Our

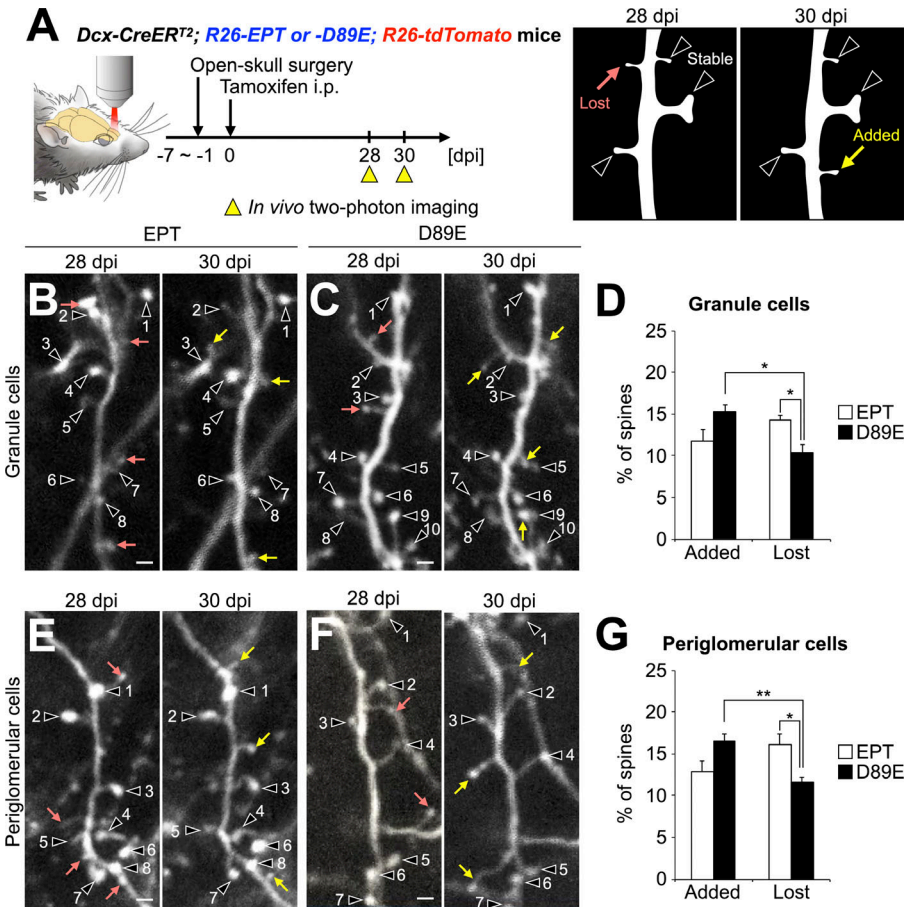

Figure 6. **PS is involved in the spine pruning of adult-born neurons in the OB. (A)** Experimental scheme. In vivo two-photon imaging of dendritic spines of tdTomato$^+$ granule and periglomerular cells in the adult *Dcx-CreER^{T2}; R26-EPT; R26-tdTomato* (*EPT*) and *Dcx-CreER^{T2}; R26-D89E; R26-tdTomato* (*D89E*) mice was performed at 28 and 30 dpi. Dendritic spines identified at 28 and 30 dpi were classified into stable (black arrowheads), lost (pink arrow), or added (yellow arrow; B, C, E, and F). **(B–G)** Effect of MFG-E8^{D89E} on dendritic spine dynamics in tdTomato$^+$ granule (B–D) and periglomerular (E–G) cells. Representative in vivo projection images of dendritic spines of granule (B and C) and periglomerular (E and F) cells in adult *EPT* (B, E; n = 4 mice) and *D89E* (C, F; n = 4 mice) mice are shown. Numbers identify spines that were maintained over the 2-d observation period. Percentages of added and lost spines of granule (D) and periglomerular (G) cells in the adult *EPT* (n = 4 mice) and *D89E* (n = 4 mice) mice are shown (Granule cells [D], $F_{group(1,6)}$ = 378.7, p_{group} = 1.2 × 10^{-6}, $F_{dynamics(1,6)}$ = 2.9, $p_{dynamics}$ = 0.90, $F_{group\times dynamics(1,6)}$ = 27.9, P = 1.9 × 10^{-3}, two-way repeated measures ANOVA; *EPT* versus *D89E*, $t_{(6)}$ = 3.2, P = 0.019 in Lost, unpaired t test; added versus lost, $t_{(3)}$ = 5.5, P = 0.012 in *D89E*, paired t test; Periglomerular cells [G], $F_{group(1,6)}$ = 332.8, p_{group} = 1.7 × 10^{-6}, $F_{dynamics(1,6)}$ = 1.5, $p_{dynamics}$ = 0.89, $F_{group\times dynamics(1,6)}$ = 43.2, P = 5.9 × 10^{-4}, two-way repeated measures ANOVA; *EPT* versus *D89E*, $t_{(6)}$ = 3.1, P = 0.021 in Lost spines, unpaired t test; added versus lost, $t_{(3)}$ = 7.4, P = 0.0050 in *D89E*, paired t test). Data are pooled from three independent experiments. Scale bars in B, C, E, F, 2 µm. *, P < 0.05; **, P < 0.01; adjusted with Bonferroni correction. Data shown are mean ± SEM.

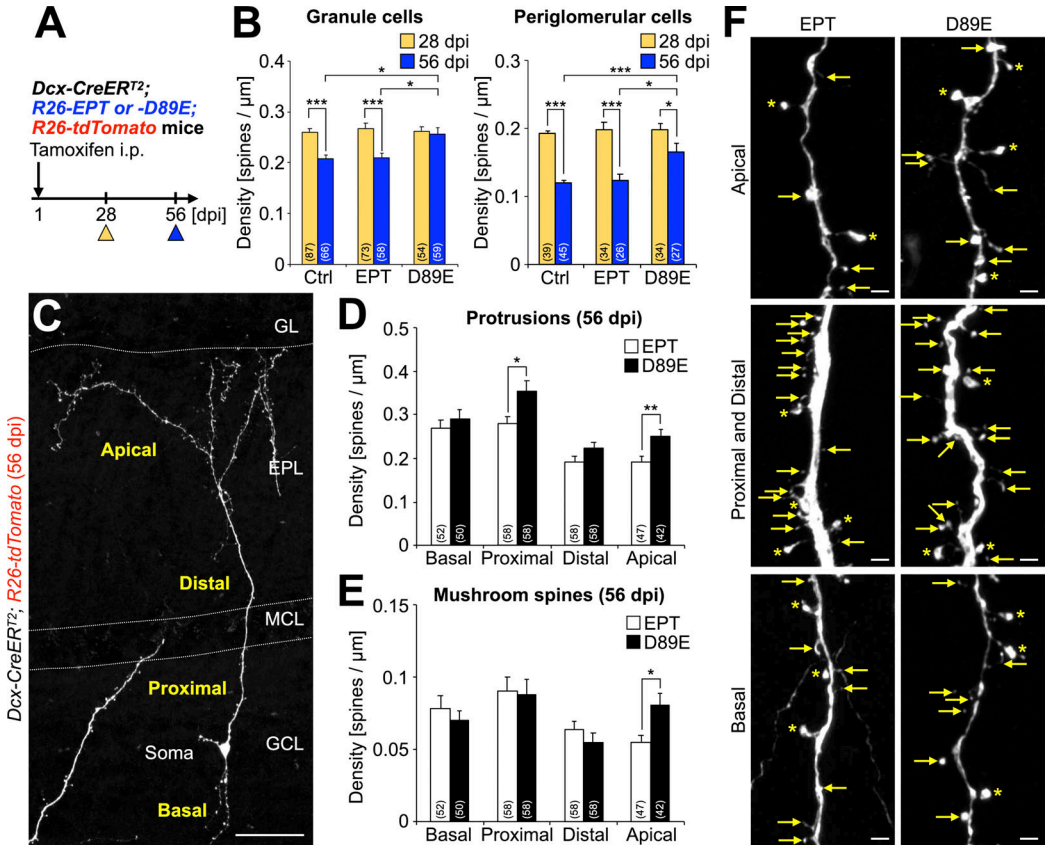

Figure 7. **Inhibition of PS-dependent spine pruning by MFG-E8^{D89E} increases the synaptic density in adult-born mature neurons in the OB. (A)** Experimental scheme. **(B)** Total protrusion density of granule and periglomerular cells in *Dcx-CreER^{T2}; R26-tdTomato* (Ctrl), *Dcx-CreER^{T2}; R26-EPT; R26-tdTomato* (*EPT*), and *Dcx-CreER^{T2}; R26-D89E; R26-tdTomato* (*D89E*) mice at 28 and 56 dpi (Ctrl, $n = 4$ [28 dpi] and 3 [56 dpi] mice; *EPT*, $n = 3$ [28 dpi] and 4 [56 dpi] mice; *D89E*, $n = 3$ mice [28 and 56 dpi]) (Granule cells, Ctrl, 28 dpi versus 56 dpi, $t_{(151)} = 5.6$, $P = 9.2 \times 10^{-8}$, unpaired *t* test; *EPT*, 28 dpi versus 56 dpi, $t_{(129)} = 6.0$, $P = 1.7 \times 10^{-8}$, unpaired *t* test; 56 dpi, $x^2_{(2)} = 10.7$, $P = 0.0048$, Ctrl versus *D89E*, $P = 0.015$, *EPT* versus *D89E*, $P = 0.013$, Steel-Dwass test; periglomerular cells, Ctrl, 28 dpi versus 56 dpi, $t_{(82)} = 11.4$, $P = 2.2 \times 10^{-16}$, unpaired *t* test; *EPT*, 28 dpi versus 56 dpi, $t_{(58)} = 5.0$, $P = 5.8 \times 10^{-6}$, unpaired *t* test; *D89E*, 28 dpi versus 56 dpi, $t_{(59)} = 2.0$, $P = 0.045$, unpaired *t* test; 56 dpi, $x^2_{(2)} = 11.7$, $P = 0.0029$, Ctrl versus *D89E*, $P = 0.0023$, *EPT* versus *D89E*, $P = 0.032$, Steel-Dwass test). Data are pooled from eight independent experiments. **(C)** Representative image of tdTomato$^+$ granule cells of adult *Dcx-CreER^{T2}; R26-tdTomato* mice at 56 dpi ($n = 3$ mice) stained for DsRed (white). Dendrites of granule cells are divided into four subregions: apical, distal, proximal, and basal. **(D–F)** Effect of MFG-E8^{D89E} on the spine density of granule cells in the OB. Density (D [Proximal, $P = 0.012$, Welch's *t* test; Apical, $t_{(88)} = -2.9$, $P = 0.0051$, unpaired *t* test], E [Apical, $P = 0.011$, Welch's *t* test]) and representative images (F) of protrusions (D) and mushroom spines (E) in the granule cells in *EPT* ($n = 4$ mice) and *D89E* ($n = 3$ mice) mice 56 dpi are shown. Asterisks and arrows indicate mushroom spines and other protrusions, respectively (F). Data are pooled from four independent experiments. Parentheses in B, D, and E indicate the number of analyzed cells. GCL, granule cell layer; MCL, mitral cell layer; EPL, external plexiform layer; GL, glomerular layer. Scale bars: C, 50 µm; F, 2 µm. *, $P < 0.05$; **, $P < 0.01$; ***, $P < 0.005$. Data shown are mean ± SEM.

results support the idea that synaptic PS acts as an eat-me signal for microglia in adult-born neurons in the OB and DG.

During dead cell clearance by phagocytosis, targeted cells are first touched, then wrapped, and finally phagocytosed by phagocytes. PS is involved in the wrapping and subsequent phagocytosis of targeted cells by promoting the spreading of phagocytes' plasma membrane (Freeman and Grinstein, 2014; Segawa and Nagata, 2015; Nagata and Segawa, 2021; Lemke, 2019). Previous EM analyses have revealed that microglia also contact synapses to monitor their state and can engulf them (Wake et al., 2009; Tremblay et al., 2010; Weinhard et al., 2018; Savage et al., 2020). However, how microglia phagocytose synapses and whether PS is involved in these processes have not been precisely understood. Our SBF-SEM analyses and in vivo two-photon imaging suggest a sequential transition in the status of microglia-spine association from the touching step to phagocytosis. Therefore, the mechanism for microglial phagocytosis of spines resembles that of macrophage's phagocytosis of dead cells (Freeman and Grinstein, 2014; Lemke, 2019; Nagata and Segawa, 2021). Inactivation of flippases and/or activation of scramblases, which induce the exposure of PS at the surface of dead cells (Segawa et al., 2016, 2014; Suzuki et al., 2016, 2013), live cells (Park et al., 2021), and degenerating dendrites (Sapar et al., 2018), may also be involved in its synaptic exposure. Decreased microglial spreading on, wrapping of, and phagocytosis of spines in *D89E* mice suggest that PS promotes the spreading of microglial membranes over the spines. Thus, we conclude that the PS-mediated promotion of phagocytes' membrane spreading on targets is a mechanism common to dead cell clearance and spine removal by phagocytosis.

Multiple synaptic eat-me signals, PS and complement components, localized in a subset of spines, contribute to their

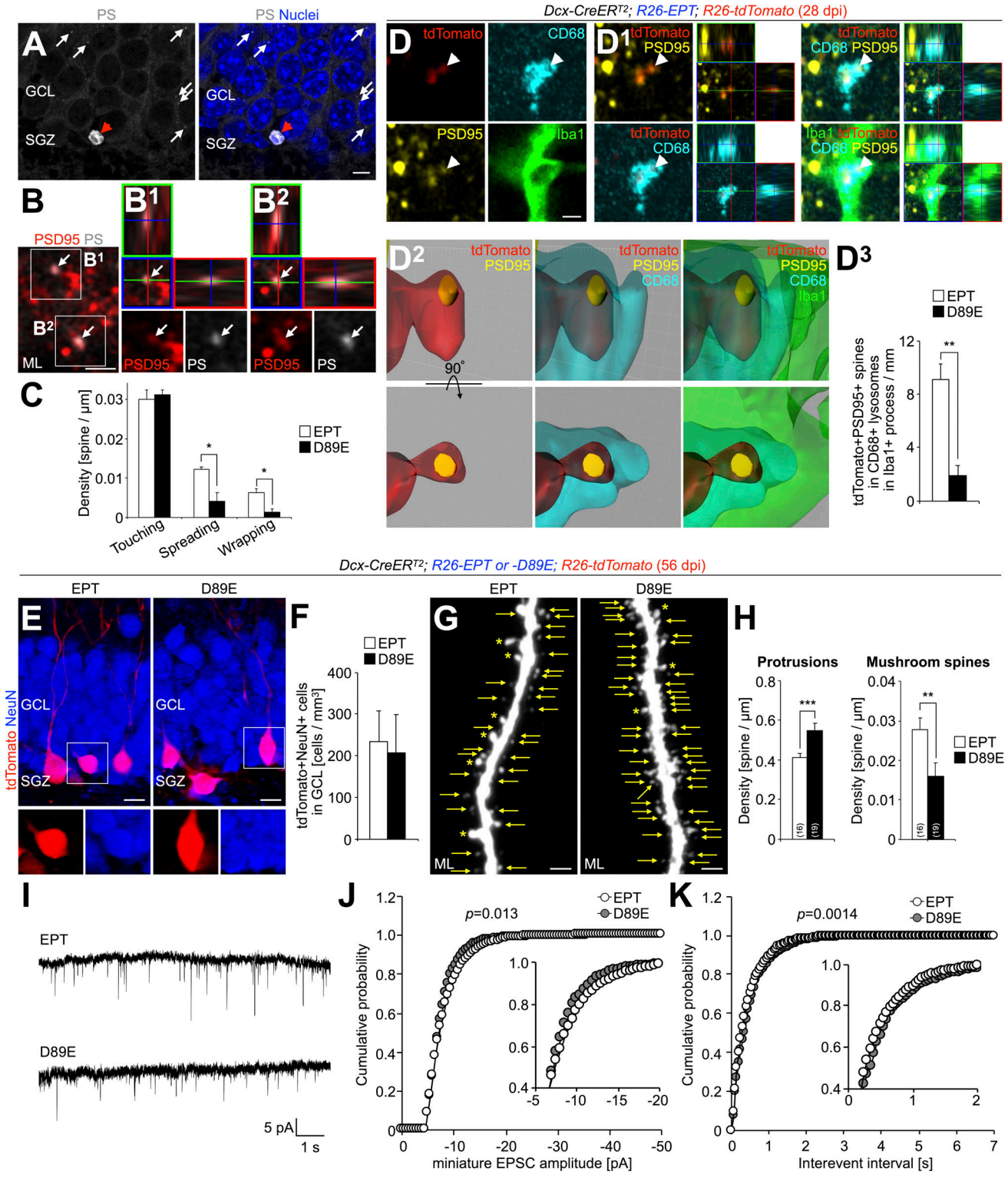

Figure 8. **Inhibition of PS-dependent spine pruning by MFG-E8^{D89E} disrupts the synaptic maturation of adult-born neurons in the hippocampal DG.** **(A)** Representative image of the DG in the hippocampus of adult WT mice injected with PSVue480 (white; *n* = 4 mice). White arrows and red arrowheads indicate PS$^+$ dots and a pyknotic cell, respectively. Nuclei are stained by Hoechst 33342 (blue). **(B)** Representative images of the ML of adult WT mice injected with PSVue480 (white), stained for PSD95 (red). The boxes in B are enlarged and shown by orthogonal view (B^1 and B^2). Arrows (B, B^1, and B^2) indicate PS$^+$PSD95$^+$ signals (36.3 ± 3.0% [*n* = 3 mice] of PS$^+$ dots are colocalized with PSD95; pooled from two independent experiments). **(C)** Effect of MFG-E8^{D89E} on microglial contacts to spines of adult-born neurons in the DG. The density of microglial contacts to tdTomato$^+$ spines in the adult *Dcx-CreER^{T2}; R26-EPT; R26-tdTomato* (*EPT*) and *Dcx-CreER^{T2}; R26-D89E; R26-tdTomato* (*D89E*) mice (*n* = 3 mice each) is shown (spreading, $t_{(4)}$ = 3.7, P = 0.022, unpaired *t* test; wrapping, $t_{(4)}$ = 4.0, P = 0.016, unpaired *t* test; pooled from three independent experiments). **(D)** Effect of MFG-E8^{D89E} on microglial phagocytosis of spines of adult-born neurons in the DG. Representative single z-plane (D), orthogonal (D^1), and surface-rendered 3D (D^2) images of the ML of adult *EPT* mice (*n* = 4 mice) stained for

PSD95 (yellow), CD68 (cyan), and Iba1 (green) are shown. tdTomato$^+$ signals (red) are directly observed without staining. Arrowheads indicate PSD95$^+$tdTomato$^+$ spines incorporated in CD68$^+$ lysosomes in Iba1$^+$ microglial processes (D and D^1). The percentages of PSD95$^+$tdTomato$^+$ spines incorporated in CD68$^+$ lysosomes in Iba1$^+$ microglial processes in adult *EPT* (n = 4 mice) and *D89E* (n = 3 mice) mice at 28 dpi are shown (D^3; $t_{(5)}$ = 4.7, P = 0.0054, unpaired t test; pooled from three independent experiments). Also, see Video 6. **(E and F)** Effect of MFG-E8^{D89E} on the survival of granule cells in the DG. Representative images of the DG in the hippocampus of adult *EPT* and *D89E* mice (n = 3 mice each) stained for DsRed (red) and NeuN (blue) are shown in E. Density of tdTomato$^+$NeuN$^+$ granule cells in *EPT* and *D89E* mice (n = 3 each) at 56 dpi is shown in F (pooled from three independent experiments). **(G and H)** Effect of MFG-E8^{D89E} on the spine density of granule cells in the DG. Representative images (G) and densities of protrusions (H, P = 0.0025, Welch's t test) and mushroom spines (H, $t_{(36)}$ = 2.7, P = 0.0098, unpaired t test) of dentate granule cells in *EPT* and *D89E* mice at 56 dpi (n = 3 mice each) are shown. Asterisks and arrows indicate mushroom spines and other protrusions, respectively (G). Parentheses in H indicate the number of analyzed cells. Data are pooled from two independent experiments. **(I)** Typical recordings of miniature EPSCs from tdTomato$^+$ granule cells at 65–74 dpi in *EPT* (top) and *D89E* (bottom) mice. **(J and K)** Cumulative probability distributions of miniature EPSC amplitudes (J, bins: 0.5 pA; P = 0.013, two-sample Kolmogorov–Smirnov test) and interevent intervals (K, bins: 50 ms; P = 0.0014, two-sample Kolmogorov–Smirnov test) in *EPT* (n = 8 cells from four mice, pooled from four independent experiments) and *D89E* mice (n = 6 cells from three mice, pooled from three independent experiments). SGZ, subgranular zone; GCL, granule cell layer; ML, molecular layer. Scale bars: A, 5 µm; B and D, 1 µm; G, 2 µm; E, 10 µm. *, P < 0.05; **, P < 0.01; ***, P < 0.005. Data shown are mean ± SEM.

pruning by microglia under physiological (Stevens et al., 2007; Schafer et al., 2012; Cong et al., 2020; Li et al., 2020; Scott-Hewitt et al., 2020; Park et al., 2021) and pathological conditions (Lui et al., 2016; Hong et al., 2016; Vasek et al., 2016; Dejanovic et al., 2018; Yilmaz et al., 2021; Lall et al., 2021) in the postnatal brain. Although C1q has the potential to bind to PS (Martin et al., 2012; Païdassi et al., 2008), their interaction at synapses has not been demonstrated. Future studies on C1q and C3 will clarify the significance of the relationship between complement proteins and PS in synaptic pruning. While the role of PS in synaptic pruning during postnatal brain development has been recently demonstrated (Scott-Hewitt et al., 2020; Li et al., 2020; Park et al., 2021), it remains unknown whether PS exposure is influenced by neuronal activity. Our observations suggest that PS is preferentially presented by inactive spines, and that its exposure, which is affected by odor deprivation and enrichment, is coupled with microglial phagocytosis of spines of adult-born neurons. We, therefore, propose that neuronal activity alters not only synaptogenesis (Livneh et al., 2009; Breton-Provencher et al., 2016) but also PS-mediated spine pruning, both of which contribute to functional synaptic maturation in adult-born neurons.

Roles of PS-dependent phagocytosis by microglia in spine pruning of developing adult-born neurons

In the present study, we have demonstrated that dendritic spines present PS and are phagocytosed by microglia in adult-born neurons in the OB and DG. Inactive spines with a small spine head preferentially present PS. Most of the spines wrapped by microglia are of the thin type. Therefore, these findings suggest that morphologically immature and inactive spines are labeled with PS and phagocytosed by microglia. Moreover, masking of PS by MFG-E8^{D89E} in vivo inhibited microglial phagocytosis of spines, leading to an increase in the density of total protrusions and alteration of electrophysiological properties in adult-born neurons. Although we occasionally observed partial phagocytosis of spines, which morphologically resembled trogocytosis of presynaptic elements (Weinhard et al., 2018), its significance in synapse development remains unknown. Unlike the spines of adult-born neurons, those of hippocampal CA1 neurons are not phagocytosed by microglia (Weinhard et al., 2018), suggesting that microglial spine pruning plays an important role for adult-born neurons in their integration into the surrounding preexisting circuits. These results indicate that PS-dependent spine pruning by microglia is a common mechanism for synaptic development in adult-born neurons in the OB and DG.

Besides, the OB and DG showed distinct outcomes in the synaptic development of adult-born neurons in *D89E* mice. In the OB, a decreased density of phagocytosed spines in microglial processes at 28 dpi and an increased density of mature spines at 56 dpi were both observed in the apical dendrites of granule cells, where these spines receive inputs from the dendrites of M/T cells. Considering that adult-born granule cells increase the selectivity of odor responses at 4 weeks after their birth and maintain a steady state thereafter (Wallace et al., 2017), our results suggest that PS-dependent microglial pruning of immature spines contributes to both the acquisition and maintenance of a functional maturation state of adult-born neurons by preventing the formation of excessive synapses. In contrast, in the DG, *D89E* mice showed a decrease in the number of mushroom spines and the ratio of spines with large inputs, leading to altered electrophysiological properties. These results suggest that the maturation of synapses depends on the PS-dependent pruning of immature spines by microglia in adult-born neurons in the DG. The distinct patterns of synaptic development in adult-born neurons in the OB and DG in *D89E* mice are likely attributable to the difference in terms of spine density. Since spine density in adult-born neurons in the OB is lower than in the DG, the corresponding dendrites may have the space to maintain an increased number of spines without affecting the maturation of preexisting ones. In contrast, the high density of immature spines of adult-born neurons in the DG could cause synaptic competition during the synaptic maturation process.

Although PS-dependent spine pruning had opposite effects on the spine densities in the OB and DG, it could paradoxically increase the activity of projection neurons in these two brain regions. In the OB, adult-born neurons are GABAergic interneurons, which receive excitatory inputs from M/T cells and return inhibitory outputs to suppress their activity. Our results suggest that microglia phagocytose excessive synapses in adult-born interneurons to increase the sensitivity of M/T cells, promoting their neuronal transmission to higher olfactory centers. In contrast, in the hippocampal DG, adult-born neurons are glutamatergic projection neurons, which receive excitatory inputs from the entorhinal cortex and send excitatory outputs to projection neurons in the hippocampal CA3. Our results suggest

that microglia phagocytose immature dendritic spines of adult-born projection neurons to promote synaptic maturation, thereby promoting the receptivity of entorhinal cortex-derived excitatory inputs in the ML. Furthermore, a recent study suggests that microglial phagocytosis of CA3 synapses in dentate granule cells promotes their synaptic maturation (Andoh et al., 2019). Together, these facts strongly suggest that spine pruning by microglia promotes neuronal transmission in the entorhinal cortex-dentate gyrus-CA3 circuits in the hippocampus.

R26-MFG-E8^{D89E} mice: a novel tool to inhibit PS-dependent phagocytosis

Several methodologies have been reported to study microglial functions in vivo. Although depletion and inactivation of microglia have revealed the importance of microglia and of their activity (Miyamoto et al., 2016; Reshef et al., 2017; Wallace et al., 2020; Wang et al., 2020; Szalay et al., 2016; Stevens et al., 2007; Matsuda et al., 2015), these methods cannot discriminate the respective microglial functions, including phagocytosis and cytokine secretion. *MFG-E8*–, *Mer*-, *Axl*-, and *TREM2*-KO mice showed defects in phagocytosis of cells and synapses by microglia (Fourgeaud et al., 2016; Neher et al., 2013; Filipello et al., 2018; Park et al., 2021). However, since these genes are also involved in other functions in microglia such as process dynamics (Fourgeaud et al., 2016), migration (Mazaheri et al., 2017; Tang et al., 2015), survival (Zhong et al., 2017), and induction of inflammation (Zhong et al., 2017), the phenotypes of their corresponding KO mice are not attributable solely to the defects in PS-dependent phagocytosis. Thus, in addition to these KO mice for PS recognition molecules, tools for target-cell-specific PS blocking without affecting microglia will be also beneficial for a better understanding of the PS-mediated biological processes.

The transgenic mouse line generated in this study enables us to inhibit PS-dependent phagocytosis without disrupting microglial genes. The dominant-negative MFG-E8^{D89E} inhibits PS binding to endogenous MFG-E8 (Hanayama et al., 2002; Asano et al., 2004), as well as other opsonins including Protein S and Gas6 (Fig. 2 B). However, we cannot rule out the possibility that MFG-E8^{D89E} also masks phosphatidylethanolamine (PE) exposed in vivo, since MFG-E8 binds to PE with a lower binding affinity (Hanayama et al., 2002). In the hippocampal DG, MFG-E8 is known to regulate NSC quiescence via α8β1 integrin (Zhou et al., 2018). Although MFG-E8^{EPT}, but not MFG-E8^{D89E}, is able to bind α8β1 integrin or αvβ3 integrin through its RGD motif, it did not affect phagocytosis of spines by microglia (Fig. 4 H) and that of apoptotic cells by macrophages (Asano et al., 2004). In contrast, although we could not exclude the possibility that the artificial MFG-E8^{D89E} expression nonspecifically affects cell behavior, we successfully observed the effects of MFG-E8^{D89E} on spine pruning of adult-born neurons without affecting their migration and synaptogenesis. Furthermore, *EPT* and *D89E* mice used in this study did not exhibit any defects in cell number and process distribution in microglia, supporting the idea that microglial genes are not disrupted.

In the future, by crossing driver mouse lines expressing Cre in phagocytes such as macrophages, neutrophils, and dendritic cells, *D89E* mice will be applicable to studying the PS-dependent phagocytosis in various organs. Therefore, by analyzing the phenotypes of MFG-E8^{D89E}–mediated masking of PS in various organs and tissues, novel PS-dependent biological processes may be identified. Thus, the *R26-MFG-E8^{D89E}* mouse line will certainly be a powerful tool to understand the biological significance of PS-dependent phagocytosis in vivo.

Microglial phagocytosis of synapses and neurodevelopmental disorders

The physiological relevance of our study is supported by the observation that NSCs in the V-SVZ and SGZ of human infants also generate new neurons, which are integrated into the OB, cerebral cortex, and DG (Sanai et al., 2011, 2004; Paredes et al., 2016; Sorrells et al., 2018; Tobin et al., 2019; Moreno-Jiménez et al., 2019), raising the possibility that these new neurons contribute to postnatal brain development in human. Therefore, PS-dependent spine pruning by microglia could be involved in the functional integration of newborn neurons in the postnatal human brain, and conversely, defective pruning may be related to neurodevelopmental disorders such as autism spectrum disorders (ASDs).

Previous studies reported pathological changes in microglial morphology and increased spine density in the brains of ASD patients (Tetreault et al., 2012; Morgan et al., 2010; Vargas et al., 2005; Weir et al., 2018) and rodents (Duan et al., 2014; Xu et al., 2020; Nie et al., 2018; Zhan et al., 2014). Furthermore, disrupted synaptic pruning by microglia and ASD-like behaviors are observed in both *TREM2*-KO mice (Filipello et al., 2018) and mouse offspring prenatally subjected to maternal inflammation (Andoh et al., 2019), suggesting that defective synaptic pruning by microglia could be a cause of ASDs. Interestingly, voluntary exercise reversed simultaneously these synaptic and behavioral abnormalities (Andoh et al., 2019). Further investigations on the relationship between synaptic PS, microglial synaptic pruning, and neuronal activity will contribute to the understanding of ASD pathology and the establishment of new therapies for ASDs.

In conclusion, our present study provides new insights into the mechanisms of synaptic pruning by microglia, which is an essential process for the formation of functional neural circuits in the postnatal and adult brain. Furthermore, the novel MFG-E8^{D89E}–based genetic approach described here constitutes a powerful tool for understanding the biology of PS-dependent phagocytosis in vivo.

Materials and methods

Animals

Male adult (8-wk-old) C57BL/6J (WT) mice were purchased from Japan SLC. *Dcx-CreER^{T2}* mice were provided by the Mutant Mouse Research Resource Center (stock no. 032780-MU). *R26-tdTomato* mice (stock no. 7914; The Jackson Laboratory) were provided by Dr. Masahiro Yamaguchi (Kochi Medical School, Kochi, Japan). *Iba1-EGFP* mice (Hirasawa et al., 2005) and *AiCE-Tg* mice (Kuboyama et al., 2020) have been described previously and maintained on the C57BL/6 background.

For the generation of *Rosa26-MFG-E8^{EPT}* (*R26-EPT*) and *Rosa26-MFG-E8^{D89E}* (*R26-D89E*) mice, *MFG-E8$^{EPT\ or\ D89E}$* cassettes

were inserted into the cloning site of the CTV vector (Thai et al., 2007; CAG promoter-loxP-STOP-loxP-*MFG-E8$^{EPT\ or\ D89E}$*-polyA; https://www.addgene.org/15912/). These vectors were electroporated into feeder-free KTPU8 ES cell lines derived from the TT2 ES cell line, according to the previously described method (Taniwaki et al., 2005). After neomycin selection, several ES clones, in which a single transgene was integrated into the *Rosa26* locus, were obtained. ES cells were aggregated with ICR morula as described (Ohmuraya et al., 2005). Chimeras were mated with C57BL/6N mice (Crea Japan), and germline transmission was obtained in two *R26-EPT* (*EPT-28#47* and *EPT44#28*) and two *R26-D89E* (*D89E-10#18* and *D89E-18#2*) transgenic mouse lines. *R26-EPT-28#47* and *R26-D89E-10#18* mice backcrossed at least seven times with C57BL/6J mice were used in this study. Primer sequences for genotyping were follows: EBV-Rev, 5′-GTGGTTTGTCCAAACTCATC-3′; MFG-E8-R441-422, 5′-ACGGGAGGCTAGGTTGTTGG-3′.

To obtain *Dcx-CreER^{T2}; R26-EPT; R26-tdTomato* and *Dcx-CreER^{T2}; R26-D89E; R26-tdTomato* mice, *Dcx-CreER^{T2}; R26-tdTomato* mice (Fujioka et al., 2017) were crossed with *R26-EPT* or *R26-D89E* heterozygous mice. Tamoxifen (Sigma-Aldrich, 20 mg/ml) was dissolved in a mixture of 4% dimethyl sulfoxide/6% ethanol/90% sesame oil and intraperitoneally injected into adult male *Dcx-CreER^{T2}; R26-tdTomato, Dcx-CreER^{T2}; R26-EPT or D89E; R26-tdTomato* and *Dcx-CreER^{T2}; R26-EPT or D89E; R26-tdTomato; Iba1-EGFP* mice, as described previously (Sawada et al., 2018; Fujioka et al., 2017). All mice used in this study were maintained in groups of seven animals per cage, on a 12-h light/dark cycle (08:00 and 20:00) with ad libitum access to food and water. All experiments involving live animals were performed in accordance with the guidelines and regulations of Nagoya City University, Tokushima Bunri University, and the Institute of Developmental Research, Aichi Developmental Disability Center.

Odor deprivation and enrichment

For 2- or 3-d odor deprivation, the left side of naris of adult WT and *AiCE-Tg* mice was occluded by a naris occlusion plug (Sawada et al., 2011) and with drops of adhesive, respectively. For 2-d odor enrichment, adult WT mice were exposed to an odor emanating from a tea ball hanging in a standard breeding cage, as reported previously (Kato et al., 2012). Natural aromas (anis, whole cloves, nutmeg, and cumin) were changed every 12 h for 2 d.

In vivo injection

Mice were anesthetized with an injection of a mixture of medetomidine/midazolam/butorphanol (MMB; 0.75 mg/kg, 4 mg/kg, and 5 mg/kg, respectively), and the head was immobilized on the stereotaxic stage (David Kopf Instruments; model 963) using ear bars. A 1.5 µl volume of PSVue 480 (1 mM; Molecular Targeting Technologies, Inc.), PSVue 550 (1 mM; Molecular Targeting Technologies, Inc.), AnnexinV-FITC (MBL Co., Ltd.), or MFG-E8-FITC (83 µg/ml; Haematologic Technologies, LLC) was stereotaxically injected into the OB (5.0 mm anterior, 0.9 mm lateral to bregma, and 1.5–2.0 mm deep) or hippocampal DG (1.4 mm posterior, 0.6 mm lateral to bregma, and 1.9–2.4 mm deep) of male adult *Dcx-CreER^{T2}; R26-tdTomato, Dcx-CreER^{T2}; R26-EPT; R26-tdTomato, Dcx-CreER^{T2}; R26-D89E; R26-tdTomato*, and WT mice as reported previously (Sawada et al., 2018). These mice were fixed 3 h after injection by transcardiac perfusion with 4% PFA/0.1 M phosphate buffer (PB).

Immunohistochemistry

Immunohistochemistry was performed as described previously (Sawada et al., 2018). Briefly, the mouse brain was fixed by transcardiac perfusion with 4% PFA/0.1 M PB and postfixed overnight in the same fixative. Coronal sections (50 µm thick) were prepared using a vibratome (VT-1200S; Leica) and incubated for 30 min at room temperature (RT) in blocking solution (10% normal donkey serum and 0.2% Triton X-100 in PBS). The sections were incubated overnight at 4°C with the primary antibodies on the shaker, and then for 2 h at RT with AlexaFluor-488/568/633/647- or biotin-conjugated secondary antibodies (1:500; Invitrogen) in the blocking solution. The signals were amplified using the Vectastain Elite ABC Kit (Vector Laboratories) and visualized using Tyramide Signal Amplification (Thermo Fisher Scientific). Sections were mounted using aqueous mounting medium PermaFluor (Lab Vision Corporation) and coverglass (Matsunami Glass Ind., Ltd.). Primary antibodies used in this study were as follows: rabbit anti-activated caspase-3 antibody (1:100; #9661; Cell Signaling Technology); mouse IgG anti-Bassoon antibody (1:100; ab82958; Abcam); rat anti-CD68 antibody (1:100; MCA1957; BioRad); rabbit anti-doublecortin (Dcx) antibody (1:500; #4604; Cell Signaling Technology); rabbit anti-DsRed antibody (1:1,000; 632496; Clontech); mouse IgG anti-DYKDDDK antibody (1:100; 014-22383; FUJIFILM Wako Pure Chemical Corporation); mouse IgG anti-GFAP antibody (1:500; G3893; Sigma-Aldrich); rabbit anti-GFAP antibody (1:1,000; Z0334; Dako); rat anti-GFP antibody (1:1,000; 04404-84; Nacalai Tesque, Inc.); goat anti-Iba1 antibody (1:500; ab5076; Abcam); mouse IgG anti-NeuN antibody (1:100; MAB377; Millipore); rabbit anti-postsynaptic density 95 (PSD95) antibody (1:400; ab18258; Abcam); and rabbit anti-Synaptophysin-1 antibody (1:400; 101002; Synaptic Systems). Nuclei were stained with Hoechst 33342 (1:5,000; H1399; Thermo Fisher Scientific). For PS staining of postfixed brain sections, prior to immunohistochemistry, sections were washed with TES (N-tris-[hydroxymethyl]-methyl-2-aminoethane sulfonic acid) buffer (5 mM TES, 145 mM NaCl, pH = 7.4) three times, incubated for 1.5 h at RT with 30 µM PSVue 480 or 10 µM PSVue 550 in TES buffer, and washed three times with TES buffer.

Imaging and quantification in confocal and superresolution microscopy

Z-stack images of tdTomato$^+$ neurons and Iba1$^+$ microglia in the adult OB and DG were acquired by scanning at 0.5-µm intervals using an LSM 700 confocal laser scanning microscope (Carl Zeiss) with a 40× water-immersion objective lens (NA 1.2). Images were acquired from every sixth coronal section. For quantification of the number of tdTomato$^+$ neurons in the RMS, OB, and DG, z-stack images of these cells were acquired by scanning at 2.0-µm intervals using an LSM 700 confocal laser scanning microscope with a 20× objective lens (NA 0.8). All

labeled cells in these regions of every sixth coronal section were counted. For quantification of the number of Iba1$^+$ microglia in the GCL and EPL of the adult OB, the cells were counted stereologically using a Stereo Investigator system (MBF Bioscience), as reported previously (Sawada et al., 2018). In Figs. 4 and 8, microglial contacts with spines were classified into three types based on the percentage of the area of tdTomato-labeled spines covered by Iba1$^+$ process: touching (<50%), spreading (50–90%), and wrapping (>90%). Spines were morphologically classified into three types: mushroom (>0.65-µm [for OB] or 0.5-µm [for DG] spine head width with a neck), stubby (spine head with no neck), thin (<0.65-µm [for OB] or 0.5-µm [for DG] spine head width), and filopodia (no spine head). To obtain spine density (spines per µm), the number of analyzed spines was divided by the measured dendritic length. For PSVue$^+$ staining, the criterion of puncta signal was set using adult WT brain sections stained with PSVue reagent without zinc solution. For PSD95 and synaptophysin staining, the criteria of puncta signals were set using adult WT brain sections stained without primary antibody. For synaptic puncta analyses (Figs. 2, 3, 4, 8, S2, S3, and S4), image acquisition was performed using an LSM 880 confocal laser scanning microscope with Airyscan using super-resolution mode with a 63× oil-immersion objective lens (NA 1.4; optical zoom, 1.8×, 0.050 µm per pixel), and superresolution images of at least 5 ROIs (at least 5 z-planes with 0.5 µm-interval) per animal were acquired as reported previously with modification (Whitman and Greer, 2007). Colocalization of puncta signals was analyzed using sequential two-dimensional z-planes. For three-dimensional (3D) visualization of microglial phagocytosis of adult-born neuron spines, surface-rendered 3D images were made using Imaris (Bitplane, version 7.5.2) as previously reported (Sawada et al., 2020). Only PSD95$^+$tdTomato$^+$ spines targeted in CD68$^+$ lysosomes were extracted using filter and adjusting the upper/lower limit values of the histogram (Sawada et al., 2020). All original superresolution images were acquired as 16-bit data and processed and converted into 8-bit tiff images using ZEN software (Carl Zeiss). In PSVue 480-, PSVue 550-, AnnexinV-FITC-, or MFG-E8-FITC-injection experiments, the regions >300 µm far from the injected site were analyzed. In the analysis of PS intensity, the signal intensity of PSVue480 within tdTomato$^+$ spines was measured using ZEN software. For spine analyses of *AiCE-Tg* mice with the unilateral naris occlusion, the ROIs of PSD95$^+$ spines were automatically selected using a Watershed algorithm in TI workbench and their EGFP-staining intensity was calculated, as reported previously (Kuboyama et al., 2020). "Active" spines in the naris-opened side of OB were defined here as PSD95$^+$ spines with an EGFP intensity higher than the baseline, which was automatically set as an average of 100 highest EGFP intensity in the spines of the naris-occluded side of OB in the same mice. For the active spine analysis, 45,000 PSD95$^+$ spines (1,000 brightest spines of 45 independent images from two mice) were analyzed, in which 629 were defined as active and other 44,371 spines were described as less-active spines.

SBF-SEM

SBF-SEM analyses were performed as described previously with slight modifications (Thai et al., 2016; Nguyen et al., 2016; Sawada et al., 2018; Matsumoto et al., 2019). Adult WT mouse brains were fixed by transcardiac perfusion with 2.5% GA and 2% PFA in 0.1 M PB (pH 7.4) at 4°C and postfixed in the same fixative for 2 days at 4°C. Coronal sections (200 µm thick) were prepared using a vibratome (VT-1200S; Leica), and a part of the GCL of the OB (1 × 1 mm) was dissected from these sections using an ophthalmic knife under a stereomicroscope. These blocks were treated with 2% OsO_4 and 1.5% potassium ferricyanide in PBS for 1 h at 4°C, 1% thiocarbohydrazide for 20 min at RT, 2% aqueous OsO_4 for 30 min at RT, uranyl acetate solution for O/N at 4°C, and lead aspartate solution for 2 h at 50°C. The samples were then dehydrated in a graded ethanol series (60, 80, 90, 95, and 100%) and treated with dehydrated acetone. Coronal OB sections (1 mm × 1 mm × 200 µm) were embedded in Durcupan resin containing 8% Ketjen black powder and put vertically on the rivets (Fig. S1 F) for two overnights at 60°C to ensure polymerization. SBF-SEM image acquisition of adult OB tissues was performed using a Merlin and Sigma scanning electron microscope (Carl Zeiss) equipped with a 3View in-chamber ultramicrotome system (Gatan). For microglia–synapse interaction analyses, serial image sequences were 57.2 × 57.2 µm wide (6.0 nm/pixel) and >35 µm deep at 80 nm steps. For microglial phagocytosis analyses, serial image sequences were 51.2 × 51.2 µm wide (5.0 nm/pixel) and >20 µm deep at 40 nm steps. To perform image acquisition of microglia at a high resolution, we first acquired low-magnification images of well-stained regions of a large OB area to identify cell soma possessing ultrastructural features of microglia and then high magnification images of the targeted microglia following its identification (Fig. S1 F). Sequential images were processed using FIJI software (Version 2.0.0; Rueden et al., 2017). Microglia in the SBF-SEM images were identified based on the ultrastructural features previously reported (Matsumoto et al., 2019): irregular cell contour with elongated processes, dark cytoplasm containing long endoplasmic reticulum and lysosomes, and association with extracellular spaces. Phagocytosed synaptic materials were identified by double-membrane inclusion bodies containing 40 nm vesicles within microglial processes. These inclusion bodies were either making contact with the inner surface of the plasma membrane of microglial processes associated with a granule cell dendrite or detached from the microglial plasma membrane, which were classified into early or late stages of microglial phagocytosis, respectively (Fig. 1). Segmentation of cell contours was performed using Microscopy Image Browser software (Belevich et al., 2016). For 3D reconstruction, Amira software (Maxnet Co., Ltd.) was used. Contact area between microglia and synaptic structures was analyzed using the "Surface Area Volume" tool (mode: patches) in Amira software. Microglial volume was calculated using the "Material Statistics" tool in Amira software. Event density of phagocytosis (early, late) and partial phagocytosis (early) in microglia was calculated as follows: observed event number/reconstructed microglial volume (µm^3). 22 microglia from 3 mice were analyzed in microglia–synapse interaction (Fig. S1), and 23 microglia from three mice were analyzed in microglial phagocytosis analyses (Fig. 1) in this study. Components of three-dimensional object files (.OBJ) obtained from Amira software were combined using Blender software (https://

www.blender.org/) and visualized as interactive 3D models using Sketchfab (https://sketchfab.com), as reported previously (Matsumoto et al., 2019).

In vivo two-photon imaging

In vivo two-photon imaging of new neurons in the adult OB was performed as described previously with slight modifications (Sawada et al., 2011). In open-skull surgery, adult male *Dcx-CreER^{T2}; R26-EPT or D89E; R26-tdTomato* mice and *Dcx-CreER^{T2}; R26-EPT* or *D89E; R26-tdTomato; Iba1-EGFP* mice were anesthetized with isoflurane and attached with a custom-made metal plate on their skull over the OB and cerebral cortex. The skull over the dorsal OB was removed using a high-speed drill and a microhook (10065-15; Muromachi Kikai Co., Ltd.) without damaging the dura, and two-layer cover glasses (1 × 1 mm and 2 × 2 mm; Matsunami Glass Ind., Ltd.) were attached over the OB using Vetbond (3M) and Super-Bond (Sun Medical Co., Ltd.). Two-photon imaging was performed at least four weeks after the open-skull surgery to minimize the effect of skull removal on synapse formation and pruning in new neurons in the OB. Before starting two-photon imaging, mice were anesthetized with an injection of a mixture of MMB, and the head was immobilized with a metal plate on a custom-made stage. Thinned-skull surgery has been described previously (Sawada et al., 2011). The mouse body temperature was maintained at 37°C using a heating pad during the whole two-photon imaging. Mice were injected with atipamezole (0.75 mg/kg) for recovery from MMB anesthesia and returned to their individual home cage until the next imaging.

Images of tdTomato$^+$ granule and periglomerular cells were acquired under a two-photon laser scanning microscope and mode-locked laser system at 900 nm (Mai Tai HP; Spectra-Physics) through a water-immersion objective lens (25×, NA 1.05; Nikon). Scanning and image acquisition were performed with NIS Element software version 4.40.00 (Nikon). Image stacks (1,024 × 1,024 pixels, 0.23 µm per pixel, 1-µm *z*-step size) were usually acquired (average = 4; scan speed = 0.25) from the pial surface to a depth of 150 µm (thinned skull) or 300–400 µm (open-skull technique). The same regions could be repeatedly identified based on the blood vessel map of the dorsal surface of the OB and glomerular patterns, as reported previously (Sawada et al., 2011). For in vivo two-photon time-lapse imaging in *Dcx-CreER^{T2}; R26-EPT* or *D89E; R26-tdTomato* mice, image acquisition was performed every 30 s for 30 min. For analyzing the filopodia dynamics, the acquired images were smoothened using ZEN software (Carl Zeiss). Three different *z*-plane images within 6 µm were projected in Fig. 6 to maximize the signals of dendrites and spines. Analysis of spine dynamics was performed as described previously (Sailor et al., 2016). Spines were classified into three types: added, lost, and stable. Proportions of added and lost spines over two days were calculated as follows: $\%_{\text{added or lost}} = \text{Number}_{\text{added or lost}}/\text{Number}_{\text{total [added+lost+stable]}}$ (Sailor et al., 2016).

Time-lapse images of tdTomato$^+$ granule cells and EGFP$^+$ microglia in *Dcx-CreER^{T2}; R26-EPT or D89E; R26-tdTomato; Iba1-EGFP* mice were acquired under a two-photon laser scanning microscope and mode-locked laser system at 950 nm through a water-immersion objective lens (25×, NA 1.05). Image stacks (1,024 × 1,024 pixels, 0.10 µm per pixel, 0.50-µm *z*-step size) were usually acquired (average = 2; scan speed = 0.5) with an interval of 1.5 min for 60–120 min. Time-lapse images of single *z*-plane images were shown in Fig. 5. Microglial touching and wrapping of spines were classified based on the area of tdTomato-labeled spines covered by Iba1$^+$ process similar to the histological analyses in Fig. 4. Raw z-stack images without any filtration were used for the analyses of microglia–spine interaction. "Spreading" events were included in "wrapping" in this analysis because these two classes were indistinguishable due to limited resolution. Frequency of microglial touching to, wrapping of, and phagocytosis of spines was calculated as follows: Freq = Number of events/imaging duration [min] per animal.

Brain slice preparation and electrophysiology

Brain slices were prepared from mice 65–74 days after an intraperitoneal injection of tamoxifen. Mice were sacrificed by cervical spine dislocation. Brains were quickly removed, and coronal 300-µm-thick slices were cut using a vibratome in ice-cold modified artificial cerebrospinal fluid (ACSF) containing 206 mM sucrose, 5 mM KCl, 8 mM $MgCl_2$, 1.25 mM KH_2PO_4, 1 mM $CaCl_2$, 26 mM $NaHCO_3$, and 10 mM D-glucose. ACSF was gassed with 95% O_2/5% CO_2, and the pH was adjusted to 7.4. Slices were maintained for at least 1.5 h at RT (26–28°C) in an incubation chamber containing gassed standard ACSF containing 128 mM NaCl, 5 mM KCl, 1.3 mM $MgSO_4$, 1.25 mM KH_2PO_4, 2.41 mM $CaCl_2$, 26 mM $NaHCO_3$, and 10 mM D-glucose.

A single brain slice was transferred to the recording chamber where it was superfused continuously with gassed standard ACSF at a rate of 2–2.5 ml/min at 30–31°C. For whole-cell patch-clamp recordings from tdTomato$^+$ dentate granule cells, a patch electrode was filled with a pipette solution containing 140 mM K gluconate, 10 mM KCl, 2 mM $MgCl_2$, 0.2 mM EGTA, 10 mM Hepes, 3 mM Mg-ATP, and 0.3 mM Na-GTP (pH 7.2), with a resistance of 6–8 MΩ. IR-DIC optics and fluorescence microscopy (BX51WI with 40× water-immersion objective lens; Olympus Corporation) were used to image tdTomato$^+$ dentate granule cells. Holding potentials were compensated for the junction potential between the pipette solution and the external solution. Resting membrane potentials were measured in current-clamp mode (I = 0 pA). Depolarizing current steps (50 pA steps, 0–450 pA; 100 ms duration) were applied to measure the maximum number of action potentials. Miniature excitatory postsynaptic currents (EPSCs) were recorded in voltage-clamp mode at a membrane potential of −70 mV and in the presence of the voltage-dependent Na^+ channel blocker (1 µM tetrodotoxin) and $GABA_A$ receptor antagonist (20 µM bicuculline methiodide). Access resistance was monitored continuously during the experiment, and the obtained data were discarded if the access resistance fluctuated over 20%. Signals were amplified and filtered at 1 or 5 kHz with an amplifier (Axopatch 200B; Axon Instruments). Data acquisition and analysis were performed using pCLAMP 9.0 software (Axon Instruments). Miniature EPSCs were identified by setting the event detection threshold at 5 pA and by checking that the events had faster rising time than the decay time.

Statistics

The experiments were not randomized, and sample sizes were chosen based on previous studies. For the analyses of MFG-E8-FITC binding to spines (Fig. 2, F–I) and microglial contact and phagocytosis of spines (Fig. 4 and Fig. 8, C and D) and in vivo two-photon imaging (Figs. 5 and 6), investigators were blinded during quantification. The normality of the data was analyzed by the Kolmogorov–Smirnov test. For normally distributed data, the equality of variances was examined by *F* test, and comparison of means between two independent groups was performed by unpaired *t* test. For comparisons among multiple groups, the data were analyzed by one-way, two-way, or repeated-measures ANOVA, followed by the post hoc Tukey–Kramer test, Dunnett's test, or unpaired *t* test with Bonferroni correction, respectively. The cumulative probability distributions of the miniature EPSC amplitudes and interevent intervals were compared using the two-sample Kolmogorov–Smirnov test. All statistical analyses, except those for *AiCE-Tg* mice and electrophysiology, were performed using EZR software (Kanda, 2013), as reported previously (Sawada et al., 2018; Fujikake et al., 2018; Matsumoto et al., 2019). Fisher's exact test and one-sample and two-sample Kolmogorov–Smirnov tests were performed with R version 3.5.0. Gaussian fitting curves for the distribution of microglia-synapse adhesion areas (Fig. S1 E) and PS intensity (Fig. S2 E) were created based on the minimum value of Akaike's information criterion (AIC) using the Solver add-in tool in Excel (Microsoft) as reported previously (Sawada et al., 2018). In the analysis of microglia-synapse adhesion areas, trimodal distribution showed a minimum AIC (bimodal fitting, AIC = 298.2; trimodal fitting, AIC = 247.1; tetramodal fitting, AIC = 316.1). All numerical data were two-sided and are shown as the mean ± SEM. A P value <0.05 was considered statistically significant.

Online supplemental material

Fig. S1 shows quantitative analysis of microglia-synapse contacts and high-resolution imaging of dendrodendritic synapses in the OB by SBF-SEM. Fig. S2 shows the characterization of *EPT* and *D89E* mice used in this study. Fig. S3 shows that PSVue detects PS exposed at spines in the adult OB and DG. Fig. S4 shows subcellular domain-specific regulation of PS exposure and microglial contacts of spines of adult-born neurons. Fig. S5 shows in vivo two-photon time-lapse imaging of filopodium formation and retraction of adult-born neurons in the OB. Videos 1 and 2 show 3D reconstruction of microglia in the process of phagocytosis (early) and partial phagocytosis (early) in the adult OB, respectively. Videos 4 and 5 show representative video of in vivo time-lapse imaging of adult-born neurons and microglia in the OB of *Dcx-CreER^{T2}; R26-EPT; R26-tdTomato; Iba1-EGFP* mice and *Dcx-CreER^{T2}; R26-D89E; R26-tdTomato; Iba1-EGFP* mice, respectively. Videos 3 and 6 show surface-rendered 3D reconstructions of PSD95$^+$tdTomato$^+$ spines within CD68$^+$ lysosomes in Iba1$^+$ microglial processes in the adult OB and DG, respectively.

Acknowledgments

We are grateful to S. Nagata (Osaka University, Japan) for his valuable suggestions and advice regarding the use of MFG-E8 mutants and thoughtful comments on the manuscript. We also thank J. Suzuki (Kyoto University, Japan) for critical reading of the manuscript; M. Yamaguchi (Kochi Medical School, Japan) for materials; T. Miyamoto, H. Hida, H. Takase, N. Dohi, M. Tanaka (Nagoya City University, Japan), M. Furuse, A. Imai, M. Agetsuma, M. Narushima (National Institute of Physiological Sciences, Japan), M. Yuzaki, E. Miura (Keio University, Japan) for technical support; K. Kimura, C. Wen (Nagoya City University, Japan), and Sawamoto laboratory members for discussions; and F. Renault-Mihara, from Clearbioediting (www.clearbioediting.com), for editing a draft of this manuscript.

This work was supported by research grants from Japan Agency for Medical Research and Development (AMED; 21gm1210007 [to K. Sawamoto]), Japan Society for the Promotion of Science (JSPS) KAKENHI (26250019, 26640046, 15H01217, 15H01384, 17H01392, 17H05750, 17H05512, 19H04757, 19H04785, 18KK0213, 20H05700 [to K. Sawamoto], 26830014, 18K14823, 21K06395 [to M. Sawada], and 16H06280 [to K. Sawamoto and M. Sawada]), Bilateral Open Partnership Joint Research Projects (to K. Sawamoto), Grant-in-Aid for Research at Nagoya City University (to K. Sawamoto), Cooperative Study Programs of National Institute for Physiological Sciences (217, 227, 209, 222, 19-222, 19-234, 20-226, 20-247, 21-224, 21-243 [to K. Sawamoto]), the Mitsubishi Foundation (to K. Sawamoto), the Canon Foundation (to K. Sawamoto), and the Takeda Science Foundation (to K. Sawamoto and M. Sawada).

Author contributions: C. Kurematsu, M. Sawada, M. Ohmuraya, Mo. Tanaka, K. Kuboyama, T. Ogino, M. Matsumoto, H. Oishi, H. Inada, Y. Ishido, Y. Sakakibara, H.B. Nguyen, T.Q. Thai, and M.K. Yamada performed experiments. C. Kurematsu, M. Sawada, Mo. Tanaka, K. Kuboyama, S. Kohsaka, N. Ohno, M.K. Yamada, M. Asai, M. Sokabe, J. Nabekura, K. Asano, Ma. Tanaka, and K. Sawamoto analyzed data. C. Kurematsu, M. Sawada, Mo. Tanaka, and K. Sawamoto wrote the manuscript.

Disclosures: The authors declare no competing interests exist.

Submitted: 7 November 2020
Revised: 13 August 2021
Accepted: 30 November 2021

References

Andoh, M., K. Shibata, K. Okamoto, J. Onodera, K. Morishita, Y. Miura, Y. Ikegaya, and R. Koyama. 2019. Exercise reverses behavioral and synaptic abnormalities after maternal inflammation. *Cell Rep.* 27: 2817–2825.e5. https://doi.org/10.1016/j.celrep.2019.05.015

Asano, K., M. Miwa, K. Miwa, R. Hanayama, H. Nagase, S. Nagata, and M. Tanaka. 2004. Masking of phosphatidylserine inhibits apoptotic cell engulfment and induces autoantibody production in mice. *J. Exp. Med.* 200:459–467. https://doi.org/10.1084/jem.20040342

Belevich, I., M. Joensuu, D. Kumar, H. Vihinen, and E. Jokitalo. 2016. Microscopy image browser: A platform for segmentation and analysis of multidimensional datasets. *PLoS Biol.* 14:e1002340. https://doi.org/10.1371/journal.pbio.1002340

Breton-Provencher, V., K. Bakhshetyan, D. Hardy, R.R. Bammann, F. Cavarretta, M. Snapyan, D. Côté, M. Migliore, and A. Saghatelyan. 2016. Principal cell activity induces spine relocation of adult-born interneurons in the olfactory bulb. *Nat. Commun.* 7:12659. https://doi.org/10.1038/ncomms12659

Breton-Provencher, V., D. Cote, and A. Saghatelyan. 2014. Activity of the principal cells of the olfactory bulb promotes a structural dynamic on

the distal dendrites of immature adult-born granule cells via activation of NMDA receptors. *J. Neurosci.* 34:1748–1759. https://doi.org/10.1523/JNEUROSCI.3013-13.2014

Burk, K., A. Desoeuvre, C. Boutin, M.A. Smith, S. Kroger, A. Bosio, M.-C. Tiveron, and H. Cremer. 2012. Agrin-signaling is necessary for the integration of newly generated neurons in the adult olfactory bulb. *J. Neurosci.* 32:3759–3764. https://doi.org/10.1523/JNEUROSCI.4906-11.2012

Cong, Q., B.M. Soteros, M. Wollet, J.H. Kim, and G. M. Sia. 2020. The endogenous neuronal complement inhibitor SRPX2 protects against complement-mediated synapse elimination during development. *Nat. Neurosci.* 23:1067–1078. https://doi.org/10.1038/s41593-020-0672-0

Dejanovic, B., M.A. Huntley, A. De Mazière, W.J. Meilandt, T. Wu, K. Srinivasan, Z. Jiang, V. Gandham, B.A. Friedman, H. Ngu, et al. 2018. Changes in the synaptic proteome in tauopathy and rescue of tau-induced synapse loss by C1q antibodies. *Neuron*. 100:1322–1336.e7. https://doi.org/10.1016/j.neuron.2018.10.014

Denizet, M., L. Cotter, P.M. Lledo, and F. Lazarini. 2017. Sensory deprivation increases phagocytosis of adult-born neurons by activated microglia in the olfactory bulb. *Brain Behav. Immun.* 60:38–43. https://doi.org/10.1016/j.bbi.2016.09.015

Diaz-Aparicio, I., I. Paris, V. Sierra-Torre, A. Plaza-Zabala, N. Rodríguez-Iglesias, M. Márquez-Ropero, S. Beccari, P. Huguet, O. Abiega, E. Alberdi, et al. 2020. Microglia actively remodel adult hippocampal neurogenesis through the phagocytosis secretome. *J. Neurosci.* 40:1453–1482. https://doi.org/10.1523/JNEUROSCI.0993-19.2019

Duan, Y., S.-H. Wang, J. Song, Y. Mironova, G.l. Ming, A.L. Kolodkin, and R.J. Giger. 2014. Semaphorin 5A inhibits synaptogenesis in early postnatal- and adult-born hippocampal dentate granule cells. *Elife*. 3. https://doi.org/10.7554/eLife.04390

Filipello, F., R. Morini, I. Corradini, V. Zerbi, A. Canzi, B. Michalski, M. Erreni, M. Markicevic, C. Starvaggi-Cucuzza, K. Otero, et al. 2018. The microglial innate immune receptor TREM2 is required for synapse elimination and normal brain connectivity. *Immunity*. 48:979–991.e8. https://doi.org/10.1016/j.immuni.2018.04.016

Fourgeaud, L., P.G. Traves, Y. Tufail, H. Leal-Bailey, E.D. Lew, P.G. Burrola, P. Callaway, A. Zagorska, C. V. Rothlin, A. Nimmerjahn, et al. 2016. TAM receptors regulate multiple features of microglial physiology. *Nature*. 532:240–244. https://doi.org/10.1038/nature17630

Freeman, S.A., and S. Grinstein. 2014. Phagocytosis: Receptors, signal integration, and the cytoskeleton. *Immunol. Rev.* 262:193–215. https://doi.org/10.1111/imr.12212

Fricker, M., J.J. Neher, J.-W. Zhao, C. Thery, A.M. Tolkovsky, and G.C. Brown. 2012. MFG-E8 mediates primary phagocytosis of viable neurons during neuroinflammation. *J. Neurosci.* 32:2657–2666. https://doi.org/10.1523/JNEUROSCI.4837-11.2012

Fujikake, K., M. Sawada, T. Hikita, Y. Seto, N. Kaneko, V. Herranz-Perez, N. Dohi, N. Homma, S. Osaga, Y. Yanagawa, et al. 2018. Detachment of chain-forming neuroblasts by fyn-mediated control of cell–cell adhesion in the postnatal brain. *J. Neurosci.* 38:4598–4609. https://doi.org/10.1523/JNEUROSCI.1960-17.2018

Fujioka, T., N. Kaneko, I. Ajioka, K. Nakaguchi, T. Omata, H. Ohba, R. Fässler, J.M. García-Verdugo, K. Sekiguchi, N. Matsukawa, and K. Sawamoto. 2017. β1 integrin signaling promotes neuronal migration along vascular scaffolds in the post-stroke brain. *EBioMedicine*. 16:195–203. https://doi.org/10.1016/j.ebiom.2017.01.005

Fuller, A.D., and L.J. Van Eldik. 2008. MFG-E8 regulates microglial phagocytosis of apoptotic neurons. *J. Neuroimmune Pharmacol.* 3:246–256. https://doi.org/10.1007/s11481-008-9118-2

Gao, A., F. Xia, A.J. Guskjolen, A.I. Ramsaran, A. Santoro, S.A. Josselyn, and P.W. Frankland. 2018. Elevation of hippocampal neurogenesis induces a temporally graded pattern of forgetting of contextual fear memories. *J. Neurosci.* 38:3190–3198. https://doi.org/10.1523/JNEUROSCI.3126-17.2018

Hanayama, R., M. Tanaka, K. Miwa, A. Shinohara, A. Iwamatsu, and S. Nagata. 2002. Identification of a factor that links apoptotic cells to phagocytes. *Nature*. 417:182–187. https://doi.org/10.1038/417182a

Hardy, D., S. Malvaut, V. Breton-Provencher, and A. Saghatelyan. 2018. The role of calretinin-expressing granule cells in olfactory bulb functions and odor behavior. *Sci. Rep.* 8:9385. https://doi.org/10.1038/s41598-018-27692-8

Hirasawa, T., K. Ohsawa, Y. Imai, Y. Ondo, C. Akazawa, S. Uchino, and S. Kohsaka. 2005. Visualization of microglia in living tissues using Iba1-EGFP transgenic mice. *J. Neurosci. Res.* 81:357–362. https://doi.org/10.1002/jnr.20480

Hong, S., V.F. Beja-Glasser, B.M. Nfonoyim, A. Frouin, S. Li, S. Ramakrishnan, K.M. Merry, Q. Shi, A. Rosenthal, B.A. Barres, et al. 2016. Complement and microglia mediate early synapse loss in Alzheimer mouse models. *Science*. 352:712–716. https://doi.org/10.1126/science.aad8373

Huang, Y.-B., C.-R. Hu, L. Zhang, W. Yin, and B. Hu. 2015. In vivo study of dynamics and stability of dendritic spines on olfactory bulb interneurons in Xenopus laevis tadpoles. *PLoS One*. 10:e0140752. https://doi.org/10.1371/journal.pone.0140752

Johnston, D., and D.G. Amaral. 2004. Hippocampus. In The Synaptic Organization of the Brain. G. Shepherd, editor. Oxford, New York. 455–498

Kanda, Y. 2013. Investigation of the freely available easy-to-use software "EZR" for medical statistics. *Bone Marrow Transpl.* 48:452–458. https://doi.org/10.1038/bmt.2012.244

Kato, Y., N. Kaneko, M. Sawada, K. Ito, S. Arakawa, S. Murakami, and K. Sawamoto. 2012. A subtype-specific critical period for neurogenesis in the postnatal development of mouse olfactory glomeruli. *PLoS One*. 7:e48431. https://doi.org/10.1371/journal.pone.0048431

Kitanishi, T., J. Sakai, S. Kojima, Y. Saitoh, K. Inokuchi, M. Fukaya, M. Watanabe, N. Matsuki, and M.K. Yamada. 2010. Activity-dependent localization in spines of the F-actin capping protein CapZ screened in a rat model of dementia. *Genes to Cells*. 15:737–747. https://doi.org/10.1111/j.1365-2443.2010.01411.x

Koopman, G., C.P. Reutelingsperger, G.A. Kuijten, R.M. Keehnen, S.T. Pals, and M.H. van Oers. 1994. Annexin V for flow cytometric detection of phosphatidylserine expression on B cells undergoing apoptosis. *Blood*. 84:1415–1420

Kuboyama, K., T. Inoue, Y. Hashimotodani, T. Itoh, T. Suzuki, A. Tetsuzawa, Y. Ohtsuka, R. Kinoshita, R. Takara, T. Miyazawa, et al. 2020. Traceable stimulus-dependent rapid molecular changes in dendritic spines in the brain. *Sci. Rep.* 10:15266. https://doi.org/10.1038/s41598-020-72248-4

Lall, D., I. Lorenzini, T.A. Mota, S. Bell, T.E. Mahan, J.D. Ulrich, H. Davtyan, J.E. Rexach, A.K.M.G. Muhammad, O. Shelest, et al. 2021. C9orf72 deficiency promotes microglial-mediated synaptic loss in aging and amyloid accumulation. *Neuron*. 109:2275–2291.e8. https://doi.org/10.1016/j.neuron.2021.05.020

Lemke, G. 2019. How macrophages deal with death. *Nat. Rev. Immunol.* 19:539–549. https://doi.org/10.1038/s41577-019-0167-y

Lepousez, G., A. Nissant, A.K. Bryant, G. Gheusi, C.A. Greer, and P. M. Lledo. 2014. Olfactory learning promotes input-specific synaptic plasticity in adult-born neurons. *Proc. Natl. Acad. Sci. USA*. 111:13984–13989. https://doi.org/10.1073/pnas.1404991111

Lepousez, G., A. Nissant, and P.-M. Lledo. 2015. Adult neurogenesis and the future of the rejuvenating brain circuits. *Neuron*. 86:387–401. https://doi.org/10.1016/j.neuron.2015.01.002

Li, T., B. Chiou, C.K. Gilman, R. Luo, T. Koshi, D. Yu, H.C. Oak, S. Giera, E. Johnson-Venkatesh, A.K. Muthukumar, et al. 2020. A splicing isoform of GPR56 mediates microglial synaptic refinement via phosphatidylserine binding. *EMBO J.* 39:e104136. https://doi.org/10.15252/embj.2019104136

Lim, D.A., and A. Alvarez-Buylla. 2016. The adult ventricular–subventricular zone (V-SVZ) and olfactory bulb (OB) neurogenesis. *Cold Spring Harb. Perspect. Biol.* 8:a018820. https://doi.org/10.1101/cshperspect.a018820

Livneh, Y., N. Feinstein, M. Klein, and A. Mizrahi. 2009. Sensory input enhances synaptogenesis of adult-born neurons. *J. Neurosci.* 29:86–97. https://doi.org/10.1523/JNEUROSCI.4105-08.2009

Lui, H., J. Zhang, S.R. Makinson, M.K. Cahill, K.W. Kelley, H.-Y. Huang, Y. Shang, M.C. Oldham, L.H. Martens, F. Gao, et al. 2016. Progranulin deficiency promotes circuit-specific synaptic pruning by microglia via complement activation. *Cell*. 165:921–935. https://doi.org/10.1016/j.cell.2016.04.001

Martin, M., J. Leffler, and A.M. Blom. 2012. Annexin A2 and A5 serve as new ligands for C1q on apoptotic cells. *J. Biol. Chem.* 287:33733–33744. https://doi.org/10.1074/jbc.M112.341339

Matsuda, T., N. Murao, Y. Katano, B. Juliandi, J. Kohyama, S. Akira, T. Kawai, and K. Nakashima. 2015. TLR9 signalling in microglia attenuates seizure-induced aberrant neurogenesis in the adult hippocampus. *Nat. Commun.* 6:6514. https://doi.org/10.1038/ncomms7514

Matsumoto, M., M. Sawada, D. García-González, V. Herranz-Pérez, T. Ogino, H. Bang Nguyen, T. Quynh Thai, K. Narita, N. Kumamoto, S. Ugawa, et al. 2019. Dynamic changes in ultrastructure of the primary cilium in migrating neuroblasts in the postnatal brain. *J. Neurosci.* 39:9967–9988. https://doi.org/10.1523/JNEUROSCI.1503-19.2019

Mazaheri, F., N. Snaidero, G. Kleinberger, C. Madore, A. Daria, G. Werner, S. Krasemann, A. Capell, D. Trümbach, W. Wurst, et al. 2017. TREM 2 deficiency impairs chemotaxis and microglial responses to neuronal

injury. *EMBO Rep.* 18:1186–1198. https://doi.org/10.15252/embr.201743922

Miyamoto, A., H. Wake, A.W. Ishikawa, K. Eto, K. Shibata, H. Murakoshi, S. Koizumi, A.J. Moorhouse, Y. Yoshimura, and J. Nabekura. 2016. Microglia contact induces synapse formation in developing somatosensory cortex. *Nat. Commun.* 7:12540. https://doi.org/10.1038/ncomms12540

Moreno-Jiménez, E.P., M. Flor-García, J. Terreros-Roncal, A. Rábano, F. Cafini, N. Pallas-Bazarra, J. Ávila, and M. Llorens-Martín. 2019. Adult hippocampal neurogenesis is abundant in neurologically healthy subjects and drops sharply in patients with Alzheimer's disease. *Nat. Med.* 25:554–560. https://doi.org/10.1038/s41591-019-0375-9

Morgan, J.T., G. Chana, C.A. Pardo, C. Achim, K. Semendeferi, J. Buckwalter, E. Courchesne, and I.P. Everall. 2010. Microglial activation and increased microglial density observed in the dorsolateral prefrontal cortex in autism. *Biol. Psychiatry*. 68:368–376. https://doi.org/10.1016/j.biopsych.2010.05.024

Mosher, K.I., R.H. Andres, T. Fukuhara, G. Bieri, M. Hasegawa-Moriyama, Y. He, R. Guzman, and T. Wyss-Coray. 2012. Neural progenitor cells regulate microglia functions and activity. *Nat. Neurosci.* 15:1485–1487. https://doi.org/10.1038/nn.3233

Muthusamy, N., X. Zhang, C.A. Johnson, P.N. Yadav, and H.T. Ghashghaei. 2017. Developmentally defined forebrain circuits regulate appetitive and aversive olfactory learning. *Nat. Neurosci.* 20:20–23. https://doi.org/10.1038/nn.4452

Nagata, S., and K. Segawa. 2021. Sensing and clearance of apoptotic cells. *Curr. Opin. Immunol.* 68:1–8. https://doi.org/10.1016/j.coi.2020.07.007

Neher, J.J., J.V. Emmrich, M. Fricker, P.K. Mander, C. Thery, and G.C. Brown. 2013. Phagocytosis executes delayed neuronal death after focal brain ischemia. *Proc. Natl. Acad. Sci. USA*. 110:E4098–E4107. https://doi.org/10.1073/pnas.1308679110

Nguyen, H.B., T.Q. Thai, S. Saitoh, B. Wu, Y. Saitoh, S. Shimo, H. Fujitani, H. Otobe, and N. Ohno. 2016. Conductive resins improve charging and resolution of acquired images in electron microscopic volume imaging. *Sci. Rep.* 6:23721. https://doi.org/10.1038/srep23721

Nguyen, P.T., L.C. Dorman, S. Pan, I.D. Vainchtein, R.T. Han, H. Nakao-Inoue, S.E. Taloma, J.J. Barron, A.V. Molofsky, M.A. Kheirbek, and A.V. Molofsky. 2020. Microglial remodeling of the extracellular matrix promotes synapse plasticity. *Cell*. 182:388–403.e15. https://doi.org/10.1016/j.cell.2020.05.050

Nie, X., S. Kitaoka, K. Tanaka, E. Segi-Nishida, Y. Imoto, A. Ogawa, F. Nakano, A. Tomohiro, K. Nakayama, M. Taniguchi, et al. 2018. The innate immune receptors TLR2/4 mediate repeated social defeat stress-induced social avoidance through prefrontal microglial activation. *Neuron*. 99:464–479.e7. https://doi.org/10.1016/j.neuron.2018.06.035

Ohmuraya, M., M. Hirota, M. Araki, N. Mizushima, M. Matsui, T. Mizumoto, K. Haruna, S. Kume, M. Takeya, M. Ogawa, et al. 2005. Autophagic cell death of pancreatic acinar cells in serine protease inhibitor Kazal type 3-deficient mice. *Gastroenterology*. 129:696–705. https://doi.org/10.1016/j.gastro.2005.05.057

Païdassi, H., P. Tacnet-Delorme, V. Garlatti, C. Darnault, B. Ghebrehiwet, C. Gaboriaud, G.J. Arlaud, and P. Frachet. 2008. C1q binds phosphatidylserine and likely acts as a multiligand-bridging molecule in apoptotic cell recognition. *J. Immunol.* 180:2329–2338. https://doi.org/10.4049/jimmunol.180.4.2329

Paredes, M.F., D. James, S. Gil-Perotin, H. Kim, J.A. Cotter, C. Ng, K. Sandoval, D.H. Rowitch, D. Xu, P.S. McQuillen, et al. 2016. Extensive migration of young neurons into the infant human frontal lobe. *Science*. 354:aaf7073. https://doi.org/10.1126/science.aaf7073

Park, J., Y. Choi, E. Jung, S.-H. Lee, J.-W. Sohn, and W.-S. Chung. 2021. Microglial MERTK eliminates phosphatidylserine-displaying inhibitory post-synapses. *EMBO J.* 40:e107121. https://doi.org/10.15252/embj.2020107121

Price, J.L., and T.P. Powell. 1970. The synaptology of the granule cells of the olfactory bulb. *J. Cell Sci.* 7:125–155. https://doi.org/10.1242/jcs.7.1.125

Reshef, R., E. Kudryavitskaya, H. Shani-Narkiss, B. Isaacson, N. Rimmerman, A. Mizrahi, and R. Yirmiya. 2017. The role of microglia and their CX3CR1 signaling in adult neurogenesis in the olfactory bulb. *Elife*. 6:e30809. https://doi.org/10.7554/eLife.30809

Ribeiro Xavier, A.L., B.T. Kress, S.A. Goldman, J.R. Lacerda de Menezes, and M. Nedergaard. 2015. A distinct population of microglia supports adult neurogenesis in the subventricular zone. *J. Neurosci.* 35:11848–11861. https://doi.org/10.1523/JNEUROSCI.1217-15.2015

Rodríguez-Iglesias, N., A. Sierra, and J. Valero. 2019. Rewiring of memory circuits: Connecting adult newborn neurons with the help of microglia. *Front. Cell Dev. Biol.* 7:24. https://doi.org/10.3389/fcell.2019.00024

Rueden, C.T., J. Schindelin, M.C. Hiner, B.E. DeZonia, A.E. Walter, E.T. Arena, and K.W. Eliceiri. 2017. ImageJ2: ImageJ for the next generation of scientific image data. *BMC Bioinformatics*. 18:529. https://doi.org/10.1186/s12859-017-1934-z

Sailor, K.A., M.T. Valley, M.T. Wiechert, H. Riecke, G.J. Sun, W. Adams, J.C. Dennis, S. Sharafi, G.L. Ming, H. Song, and P. M. Lledo. 2016. Persistent structural plasticity optimizes sensory information processing in the olfactory bulb. *Neuron*. 91:384–396. https://doi.org/10.1016/j.neuron.2016.06.004

Sakamoto, M., N. Ieki, G. Miyoshi, D. Mochimaru, H. Miyachi, T. Imura, M. Yamaguchi, G. Fishell, K. Mori, R. Kageyama, and I. Imayoshi. 2014. Continuous postnatal neurogenesis contributes to formation of the olfactory bulb neural circuits and flexible olfactory associative learning. *J. Neurosci.* 34:5788–5799. https://doi.org/10.1523/JNEUROSCI.0674-14.2014

Sanai, N., T. Nguyen, R.A. Ihrie, Z. Mirzadeh, H.H. Tsai, M. Wong, N. Gupta, M.S. Berger, E. Huang, J.M. García-Verdugo, et al. 2011. Corridors of migrating neurons in the human brain and their decline during infancy. *Nature*. 478:382–386. https://doi.org/10.1038/nature10487

Sanai, N., A.D. Tramontin, A. Quinones-Hinojosa, N.M. Barbaro, N. Gupta, S. Kunwar, M.T. Lawton, M.W. McDermott, A.T. Parsa, J. Manuel-Garcia Verdugo, et al. 2004. Unique astrocyte ribbon in adult human brain contains neural stem cells but lacks chain migration. *Nature*. 427:740–744. https://doi.org/10.1038/nature02301

Sapar, M.L., H. Ji, B. Wang, A.R. Poe, K. Dubey, X. Ren, J.Q. Ni, and C. Han. 2018. Phosphatidylserine externalization results from and causes neurite degeneration in Drosophila. *Cell Rep.* 24:2273–2286. https://doi.org/10.1016/j.celrep.2018.07.095

Savage, J.C., M.-K. St-Pierre, M. Carrier, H. El Hajj, S.W. Novak, M.G. Sanchez, F. Cicchetti, and M.-È. Tremblay. 2020. Microglial physiological properties and interactions with synapses are altered at presymptomatic stages in a mouse model of Huntington's disease pathology. *J. Neuroinflammation*. 17:98. https://doi.org/10.1186/s12974-020-01782-9

Sawada, M., N. Kaneko, H. Inada, H. Wake, Y. Kato, Y. Yanagawa, K. Kobayashi, T. Nemoto, J. Nabekura, and K. Sawamoto. 2011. Sensory input regulates spatial and subtype-specific patterns of neuronal turnover in the adult olfactory bulb. *J. Neurosci.* 31:11587–11596. https://doi.org/10.1523/JNEUROSCI.0614-11.2011

Sawada, M., M. Matsumoto, K. Narita, N. Kumamoto, S. Ugawa, S. Takeda, and K. Sawamoto. 2020. In vitro time-lapse imaging of primary cilium in migrating neuroblasts. *Bio. Protoc.* 10:e3823. https://doi.org/10.21769/BioProtoc.3823

Sawada, M., N. Ohno, M. Kawaguchi, S. H. Huang, T. Hikita, Y. Sakurai, H. Bang Nguyen, T. Quynh Thai, Y. Ishido, Y. Yoshida, et al. 2018. PlexinD1 signaling controls morphological changes and migration termination in newborn neurons. *EMBO J.* 37:e97404. https://doi.org/10.15252/embj.201797404

Schafer, D.P., E.K. Lehrman, A.G. Kautzman, R. Koyama, A.R. Mardinly, R. Yamasaki, R.M. Ransohoff, M.E. Greenberg, B.A. Barres, and B. Stevens. 2012. Microglia sculpt postnatal neural circuits in an activity and complement-dependent manner. *Neuron*. 74:691–705. https://doi.org/10.1016/j.neuron.2012.03.026

Scott-Hewitt, N., F. Perrucci, R. Morini, M. Erreni, M. Mahoney, A. Witkowska, A. Carey, E. Faggiani, L.T. Schuetz, S. Mason, et al. 2020. Local externalization of phosphatidylserine mediates developmental synaptic pruning by microglia. *EMBO J.* 39:e105380. https://doi.org/10.15252/embj.2020105380

Segawa, K., S. Kurata, and S. Nagata. 2016. Human type IV P-type ATPases that work as plasma membrane phospholipid flippases and their regulation by caspase and calcium. *J. Biol. Chem.* 291:762–772. https://doi.org/10.1074/jbc.M115.690727

Segawa, K., S. Kurata, Y. Yanagihashi, T.R. Brummelkamp, F. Matsuda, and S. Nagata. 2014. Caspase-mediated cleavage of phospholipid flippase for apoptotic phosphatidylserine exposure. *Science*. 344:1164–1168. https://doi.org/10.1126/science.1252809

Segawa, K., and S. Nagata. 2015. An apoptotic "eat me" signal: Phosphatidylserine exposure. *Trends Cell Biol.* 25:639–650. https://doi.org/10.1016/j.tcb.2015.08.003

Shepherd, G.M., W.R. Chen, and C.A. Greer. 2004. Olfactory bulb. In The Synaptic Organization of the Brain. G.M. Shepherd, editor. Oxford, New York. 165–216

Shigemoto-Mogami, Y., K. Hoshikawa, J.E. Goldman, Y. Sekino, and K. Sato. 2014. Microglia enhance neurogenesis and oligodendrogenesis in the early postnatal subventricular zone. *J. Neurosci.* 34:2231–2243. https://doi.org/10.1523/JNEUROSCI.1619-13.2014

Sierra, A., O. Abiega, A. Shahraz, and H. Neumann. 2013. Janus-faced microglia: Beneficial and detrimental consequences of microglial phagocytosis. *Front. Cell. Neurosci.* 7:6–22. https://doi.org/10.3389/fncel.2013.00006

Sierra, A., J.M. Encinas, J.J.P. Deudero, J.H. Chancey, G. Enikolopov, L.S. Overstreet-Wadiche, S.E. Tsirka, and M. Maletic-Savatic. 2010. Microglia shape adult hippocampal neurogenesis through apoptosis-coupled phagocytosis. *Cell Stem Cell*. 7:483–495. https://doi.org/10.1016/j.stem.2010.08.014

Song, J., R.H.J. Olsen, J. Sun, G. L. Ming, and H. Song. 2016. Neuronal circuitry mechanisms regulating adult mammalian neurogenesis. *Cold Spring Harb. Perspect. Biol.* 8:a018937. https://doi.org/10.1101/cshperspect.a018937

Sorrells, S.F., M.F. Paredes, A. Cebrian-Silla, K. Sandoval, D. Qi, K.W. Kelley, D. James, S. Mayer, J. Chang, K.I. Auguste, et al. 2018. Human hippocampal neurogenesis drops sharply in children to undetectable levels in adults. *Nature*. 555:377–381. https://doi.org/10.1038/nature25975

Stevens, B., N.J. Allen, L.E. Vazquez, G.R. Howell, K.S. Christopherson, N. Nouri, K.D. Micheva, A.K. Mehalow, A.D. Huberman, B. Stafford, et al. 2007. The classical complement cascade mediates CNS synapse elimination. *Cell*. 131:1164–1178. https://doi.org/10.1016/j.cell.2007.10.036

Sultan, S., L. Li, J. Moss, F. Petrelli, F. Cassé, E. Gebara, J. Lopatar, F.W. Pfrieger, P. Bezzi, J. Bischofberger, and N. Toni. 2015. Synaptic integration of adult-born hippocampal neurons is locally controlled by astrocytes. *Neuron*. 88:957–972. https://doi.org/10.1016/j.neuron.2015.10.037

Suzuki, J., D.P. Denning, E. Imanishi, H.R. Horvitz, and S. Nagata. 2013. Xk-related protein 8 and CED-8 promote phosphatidylserine exposure in apoptotic cells. *Science*. 341:403–406. https://doi.org/10.1126/science.1236758

Suzuki, J., E. Imanishi, and S. Nagata. 2016. Xkr8 phospholipid scrambling complex in apoptotic phosphatidylserine exposure. *Proc. Natl. Acad. Sci. USA*. 113:9509–9514. https://doi.org/10.1073/pnas.1610403113

Szalay, G., B. Martinecz, N. Lénárt, Z. Környei, B. Orsolits, L. Judák, E. Császár, R. Fekete, B.L. West, G. Katona, et al. 2016. Microglia protect against brain injury and their selective elimination dysregulates neuronal network activity after stroke. *Nat. Commun.* 7:11499. https://doi.org/10.1038/ncomms11499

Tang, Y., S. Wu, Q. Liu, J. Xie, J. Zhang, D. Han, Q. Lu, and Q. Lu. 2015. Mertk deficiency affects macrophage directional migration via disruption of cytoskeletal organization. *PLoS One*. 10:e0117787. https://doi.org/10.1371/journal.pone.0117787

Taniwaki, T., K. Haruna, H. Nakamura, T. Sekimoto, Y. Oike, T. Imaizumi, F. Saito, M. Muta, Y. Soejima, A. Utoh, et al. 2005. Characterization of an exchangeable gene trap using pU-17 carrying a stop codon-beta geo cassette. *Dev. Growth Differ.* 47:163–172. https://doi.org/10.1111/j.1440-169X.2005.00792.x

Tetreault, N.A., A.Y. Hakeem, S. Jiang, B.A. Williams, E. Allman, B.J. Wold, and J.M. Allman. 2012. Microglia in the cerebral cortex in autism. *J. Autism Dev. Disord.* 42:2569–2584. https://doi.org/10.1007/s10803-012-1513-0

Thai, T.-H., D.P. Calado, S. Casola, K.M. Ansel, C. Xiao, Y. Xue, A. Murphy, D. Frendewey, D. Valenzuela, J.L. Kutok, et al. 2007. Regulation of the germinal center response by microRNA-155. *Science*. 316:604–608. https://doi.org/10.1126/science.1141229

Thai, T.Q., H.B. Nguyen, S. Saitoh, B. Wu, Y. Saitoh, S. Shimo, Y.H.A. Elewa, O. Ichii, Y. Kon, T. Takaki, et al. 2016. Rapid specimen preparation to improve the throughput of electron microscopic volume imaging for three-dimensional analyses of subcellular ultrastructures with serial block-face scanning electron microscopy. *Med. Mol. Morphol.* 49:154–162. https://doi.org/10.1007/s00795-016-0134-7

Tobin, M.K., K. Musaraca, A. Disouky, A. Shetti, A. Bheri, W.G. Honer, N. Kim, R.J. Dawe, D.A. Bennett, K. Arfanakis, and O. Lazarov. 2019. Human hippocampal neurogenesis persists in aged adults and alzheimer's disease patients. *Cell Stem Cell*. 24:974–982.e3. https://doi.org/10.1016/j.stem.2019.05.003

Tran, T.S., M.E. Rubio, R.L. Clem, D. Johnson, L. Case, M. Tessier-Lavigne, R.L. Huganir, D.D. Ginty, and A.L. Kolodkin. 2009. Secreted semaphorins control spine distribution and morphogenesis in the postnatal CNS. *Nature*. 462:1065–1069. https://doi.org/10.1038/nature08628

Tremblay, M.-È., R.L. Lowery, and A.K. Majewska. 2010. Microglial interactions with synapses are modulated by visual experience. *PLoS Biol.* 8:e1000527. https://doi.org/10.1371/journal.pbio.1000527

Vargas, D.L., C. Nascimbene, C. Krishnan, A.W. Zimmerman, and C.A. Pardo. 2005. Neuroglial activation and neuroinflammation in the brain of patients with autism. *Ann. Neurol.* 57:67–81. https://doi.org/10.1002/ana.20315

Vasek, M.J., C. Garber, D. Dorsey, D.M. Durrant, B. Bollman, A. Soung, J. Yu, C. Perez-Torres, A. Frouin, D.K. Wilton, et al. 2016. A complement-microglial axis drives synapse loss during virus-induced memory impairment. *Nature*. 534:538–543. https://doi.org/10.1038/nature18283

Wake, H., A.J. Moorhouse, S. Jinno, S. Kohsaka, and J. Nabekura. 2009. Resting microglia directly monitor the functional state of synapses in vivo and determine the fate of ischemic terminals. *J. Neurosci.* 29:3974–3980. https://doi.org/10.1523/JNEUROSCI.4363-08.2009

Wallace, J., J. Lord, L. Dissing-Olesen, B. Stevens, and V.N. Murthy. 2020. Microglial depletion disrupts normal functional development of adult-born neurons in the olfactory bulb. *Elife*. 9:e50531. https://doi.org/10.7554/eLife.50531

Wallace, J.L., M. Wienisch, and V.N. Murthy. 2017. Development and refinement of functional properties of adult-born neurons. *Neuron*. 96:883–896.e7. https://doi.org/10.1016/j.neuron.2017.09.039

Wang, C., H. Yue, Z. Hu, Y. Shen, J. Ma, J. Li, X.-D. Wang, L. Wang, B. Sun, P. Shi, et al. 2020. Microglia mediate forgetting via complement-dependent synaptic elimination. *Science*. 367:688–694. https://doi.org/10.1126/science.aaz2288

Wang, Y., M. Cella, K. Mallinson, J.D. Ulrich, K.L. Young, M.L. Robinette, S. Gilfillan, G.M. Krishnan, S. Sudhakar, B.H. Zinselmeyer, et al. 2015. TREM2 lipid sensing sustains the microglial response in an Alzheimer's disease model. *Cell*. 160:1061–1071. https://doi.org/10.1016/j.cell.2015.01.049

Weinhard, L., G. Di Bartolomei, G. Bolasco, P. Machado, N.L. Schieber, U. Neniskyte, M. Exiga, A. Vadisiute, A. Raggioli, A. Schertel, et al. 2018. Microglia remodel synapses by presynaptic trogocytosis and spine head filopodia induction. *Nat. Commun.* 9:1228. https://doi.org/10.1038/s41467-018-03566-5

Weir, R.K., M.D. Bauman, B. Jacobs, and C.M. Schumann. 2018. Protracted dendritic growth in the typically developing human amygdala and increased spine density in young ASD brains. *J. Comp. Neurol.* 526:262–274. https://doi.org/10.1002/cne.24332

Whitman, M.C., and C.A. Greer. 2007. Synaptic integration of adult-generated olfactory bulb granule cells: Basal axodendritic centrifugal input precedes apical dendrodendritic local circuits. *J. Neurosci.* 27:9951–9961. https://doi.org/10.1523/JNEUROSCI.1633-07.2007

Xu, Z.-X., G.H. Kim, J.-W. Tan, A.E. Riso, Y. Sun, E.Y. Xu, G.-Y. Liao, H. Xu, S.-H. Lee, N.-Y. Do, et al. 2020. Elevated protein synthesis in microglia causes autism-like synaptic and behavioral aberrations. *Nat. Commun.* 11:1797. https://doi.org/10.1038/s41467-020-15530-3

Yilmaz, M., E. Yalcin, J. Presumey, E. Aw, M. Ma, C.W. Whelan, B. Stevens, S.A. McCarroll, and M.C. Carroll. 2021. Overexpression of schizophrenia susceptibility factor human complement C4A promotes excessive synaptic loss and behavioral changes in mice. *Nat. Neurosci.* 24:214–224. https://doi.org/10.1038/s41593-020-00763-8

Zhan, Y., R.C. Paolicelli, F. Sforazzini, L. Weinhard, G. Bolasco, F. Pagani, A.L. Vyssotski, A. Bifone, A. Gozzi, D. Ragozzino, and C.T. Gross. 2014. Deficient neuron-microglia signaling results in impaired functional brain connectivity and social behavior. *Nat. Neurosci.* 17:400–406. https://doi.org/10.1038/nn.3641

Zhao, C., E.M. Teng, R.G. Summers, G.-L. Ming, and F.H. Gage. 2006. Distinct morphological stages of dentate granule neuron maturation in the adult mouse hippocampus. *J. Neurosci.* 26:3–11. https://doi.org/10.1523/JNEUROSCI.3648-05.2006

Zhong, L., X.-F. Chen, T. Wang, Z. Wang, C. Liao, Z. Wang, R. Huang, D. Wang, X. Li, L. Wu, et al. 2017. Soluble TREM2 induces inflammatory responses and enhances microglial survival. *J. Exp. Med.* 214:597–607. https://doi.org/10.1084/jem.20160844

Zhou, Y., A.M. Bond, J.E. Shade, Y. Zhu, C.-H.O. Davis, X. Wang, Y. Su, K.J. Yoon, A.T. Phan, W.J. Chen, et al. 2018. Autocrine Mfge8 signaling prevents developmental exhaustion of the adult neural stem cell pool. *Cell Stem Cell*. 23:444–452.e4. https://doi.org/10.1016/j.stem.2018.08.005

JEM

Supplemental material

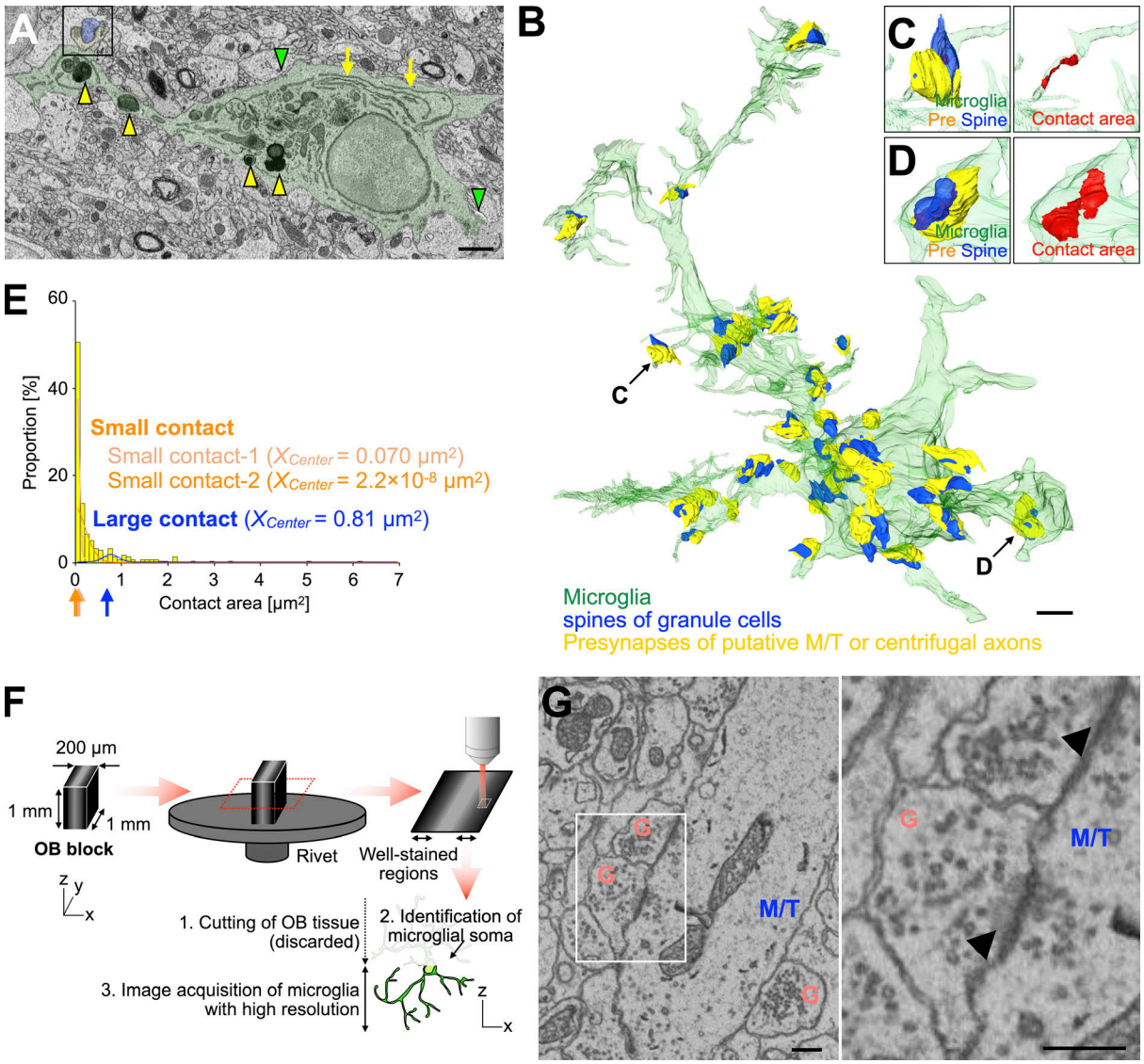

Figure S1. **Quantitative analysis of microglia-synapse contacts and high-resolution imaging of dendrodendritic synapses in the OB by SBF-SEM. (A)** Representative SBF-SEM image of microglia (green) in the GCL of the adult OB (n = 22 cells from three mice, pooled from five independent experiments). Yellow arrows, green arrowheads, and yellow arrowheads indicate long endoplasmic reticulum, extracellular space, and lysosomes, respectively. 3D reconstruction image of a synapse in the boxed area is shown in D. **(B)** 3D reconstruction of microglia in the GCL (semi-transparent green) shown in A and its associated synapses. While spines on distal, proximal, and basal dendrites of granule cells in the GCL form synapses to receive excitatory inputs from axonal terminals of mitral/tufted (M/T) cells in the OB and projection neurons in higher olfactory centers, those on apical dendrites in the EPL form dendrodendritic synapses with secondary dendrites of M/T cells (see Figs. 1 and S1 G). Presynaptic structures of putative M/T or centrifugal axons and spines of granule cells in the GCL are indicated by yellow and blue, respectively. **(C–E)** Representative three-dimensional reconstruction of small (C) and large (D) microglia-synapse contacts and distribution of microglia-synapse contact areas in the GCL (E) and corresponding gaussian fitting curves (E, trimodal distribution, AIC = 169.9, also see Materials and methods). The trimodal distribution consists of two distributions for small contacts (light orange and orange) and one distribution for large contacts (blue) and shows the minimum Akaike's information criterion (AIC) in fitting curve analysis (E, see Materials and Methods). Arrows in E under the x axis indicate the center value (X_{center}) of each fitting curve (small contact-1, light orange, X_{center} = 0.070 µm²; small contact-2, orange, X_{center} = 2.2 × 10⁻⁸ µm²; large contact, magenta, X_{center} = 0.81 µm²). Most of the contacts between microglia and synapses are classified as small contacts (C and E). At large microglia-synapse contacts, microglial processes contained lysosomes and were wrapping synaptic structures (A and D), unlike the small contact-forming microglial processes (C). Microglia, presynapses, spines, and contact area in B–D are shown in green, yellow, blue, and red, respectively. 22 cells from three mice (pooled from five independent experiments) are analyzed (E). **(F)** Experimental scheme of sample preparation and image acquisition of microglia in the adult OB for high-resolution SBF-SEM imaging. Also see Materials and methods. **(G)** Representative SBF-SEM images of dendrodendritic synapses between secondary dendrites of M/T (blue) cells and dendritic spines of granule cells (G, pink) in the EPL of the adult OB (n = 23 cells from three mice, pooled from eight independent experiments). Magnified image of boxed area (right) shows 40 nm synaptic vesicles in both M/T and granule cell spines and postsynaptic density in the granule cell spines (arrowheads). Scale bars: A and B, 2 µm; G, 400 nm.

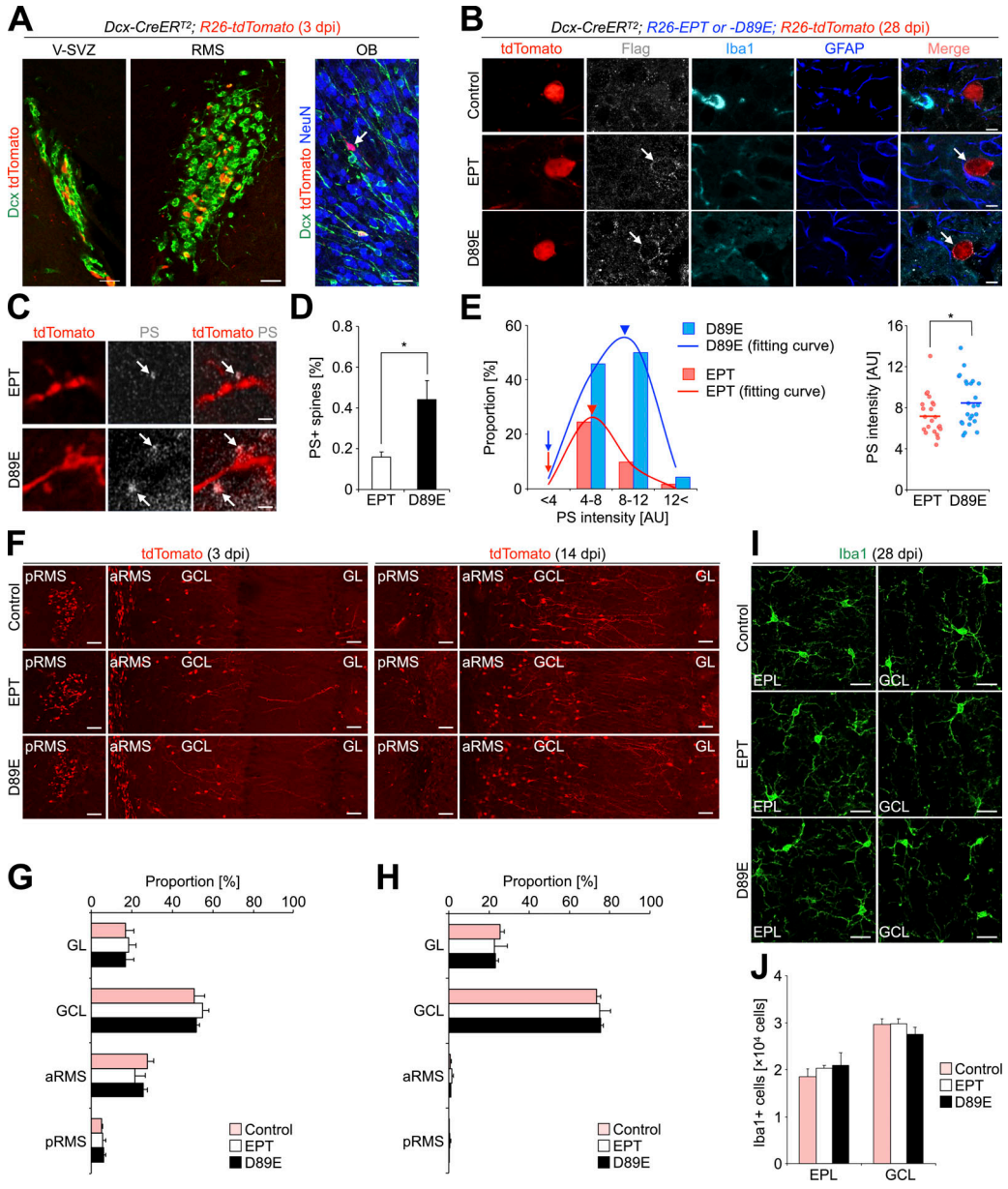

Figure S2. **Characterization of *EPT* and *D89E* mice used in this study. (A)** Representative images of the V-SVZ, RMS, and OB of adult *Dcx-CreER^{T2}; R26-tdTomato* (control) mice at 3 dpi (n = 3 mice) stained for Dcx, DsRed, and NeuN. tdTomato is expressed in the subset of Dcx$^+$ cells in the V-SVZ-RMS (10.2 ± 1.4%, n = 3 mice pooled from two independent experiments), and OB (0.7 ± 0.3%, n = 3 mice). These tdTomato$^+$ cells in the V-SVZ-OB were positive for Dcx (85.1 ± 0.8%, n = 3 mice) or NeuN (14.8 ± 0.6%, n = 3 mice), but negative for GFAP or Iba1, suggesting that some of the tdTomato$^+$ Dcx$^+$ cells were differentiated into tdTomato$^+$ NeuN$^+$ OB neurons within 3 d. **(B)** Representative images of the GCL of the OB in the adult control, *Dcx-CreER^{T2}; R26-EPT; R26-tdTomato* (*EPT*), and *Dcx-CreER^{T2}; R26-D89E; R26-tdTomato* (*D89E*) mice at 28 dpi (n = 3 mice each, pooled from six independent experiments) stained for flag (white), Iba1 (cyan), and GFAP (blue). tdTomato$^+$ signals (red) are directly observed without staining. Arrows indicate flag$^+$ signals in tdTomato$^+$ granule cells in the OB. **(C)** Representative images of the EPL of the OB in *EPT* and *D89E* mice at 28 dpi stained for DsRed (red; n = 3 mice each). Injected PSVue480 is shown in white. **(D)** Proportion of PS$^+$tdTomato$^+$ spines in the EPL of *EPT* and *D89E* mice at 28 dpi (n = 3 mice each, pooled from three independent experiments; $t_{(4)} = -3.0$, P = 0.042, unpaired t test). **(E)** Distributions (left graph, bars; and right graph) and their fitting curves (left graph, lines) of PS intensity in *EPT* and *D89E* mice at 28 dpi. Arrows and arrowheads (left graph) indicate the onset and peak of fitting curves in *EPT* (pink) and *D89E* (blue) mice (*EPT*, AIC = −55.2; *D89E*, AIC = −33.2; also see Materials and methods). While the onset of the fitting curve is similar between the two transgenic mice, its peak is shifted rightward in *D89E* mice (arrowheads, *EPT*, 8.8; *D89E*, 10.5), suggesting that PS is initially exposed on spines similarly in *EPT* and *D89E* mice, but accumulated in *D89E* mice due to the failure of the microglial spine pruning. PS intensity at tdTomato$^+$ spines in *D89E* mice (n = 24 events from three mice) is significantly higher than that in *EPT* mice (n = 22 events from three mice, pooled from three independent experiments; $t_{(44)} = -2.0$, P = 0.048, unpaired t test). **(F–H)** No effect of MFG-E8^{EPT} and MFG-E8^{D89E} on the migration of tdTomato$^+$ cells toward the OB. Representative images (F; n = 3 mice each) and proportions (G and H; pooled from four independent experiments) of tdTomato$^+$ cells (red in F) in the GL, GCL, anterior RMS (aRMS), and posterior RMS (pRMS) of control, *EPT*, and *D89E* mice at 3 (F and G) and 14 (F and H) dpi (n = 3 mice each) are shown. **(I and J)** No effect of MFG-E8^{EPT} and MFG-E8^{D89E} on the number of Iba1$^+$ microglia in the adult OB. Representative images (I; n = 3 mice each) and numbers (J; pooled from six independent experiments) of Iba1$^+$ cells (green in I) in the EPL and GCL of the OB in control, *EPT*, and *D89E* mice (n = 3 mice each) at 28 dpi are shown. RMS, rostral migratory stream; GCL, granule cell layer; EPL, external plexiform layer; GL, glomerular layer; AU, arbitrary unit. Scale bars: A and I, 20 µm; B, 5 µm; C, 1 µm; F, 50 µm. *, P < 0.05. Data shown are mean ± SEM.

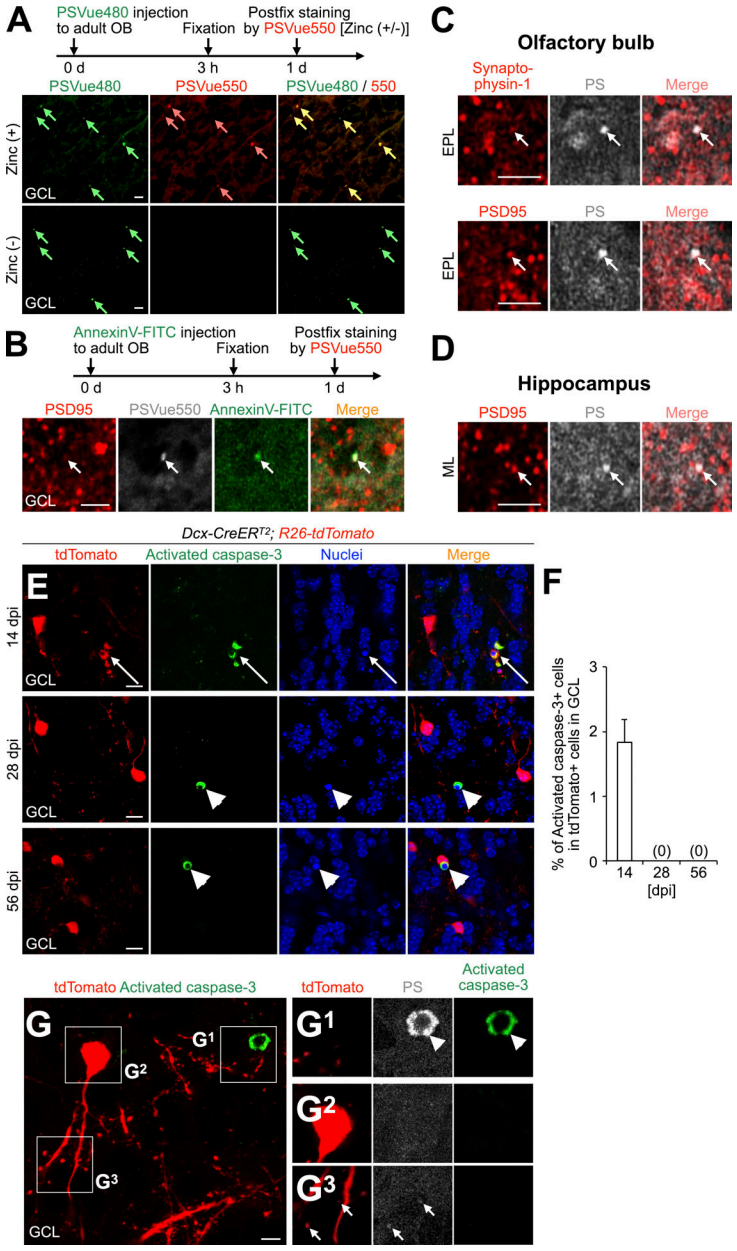

Figure S3. **PSVue detects PS exposed at spines in the adult OB and DG. (A)** Experimental scheme (top) and representative images (bottom) of the GCL of the OB in adult WT mice injected with PSVue480 (green), stained for PSVue550 (red) with or without zinc solution. PSVue480$^+$ dots (green arrows) are stained with PSVue550$^+$ dots (pink arrows) in a zinc-dependent manner (92.1 ± 1.8% [*n* = 3 mice, pooled from three independent experiments] of PSVue480$^+$ dots were colocalized with PSVue550). **(B)** Experimental scheme (top) and representative images (bottom) of the GCL of the OB in adult WT mice injected with AnnexinV-FITC (green), stained for PSVue550 (white) and PSD95 (red). Arrows indicate AnnexinV-FITC$^+$PSVue550$^+$PSD95$^+$ spines in the GCL (73.4 ± 1.1% [*n* = 3 mice, pooled from two independent experiments] of AnnexinV-FITC$^+$PSD95$^+$ dots were colocalized with PS). **(C and D)** Representative images of the EPL of the OB (C) or ML of the hippocampus (D) in adult WT mice stained for PSVue480 (PS, white) and Synaptophysin-1 (red in C, top) or PSD95 (red in C, bottom, and D). Arrows indicate double-positive signals (C, 37.9 ± 2.2% and 36.8 ± 1.4% [*n* = 3 mice, pooled from two independent experiments] of PS$^+$ dots is colocalized with Synaptophysin-1 and PSD95, respectively; D, 33.6 ± 0.9% [*n* = 3 mice, pooled from two independent experiments] of PS$^+$ dots is colocalized with PSD95). **(E and F)** Active apoptosis of tdTomato$^+$ granule cells in the adult OB. Representative images of the GCL of the OB in *Dcx-CreER^{T2}; R26-tdTomato* mice at 14, 28, and 56 dpi (*n* = 3 mice) stained for activated caspase-3 (green) are shown. tdTomato$^+$ signals (red) are directly observed without staining. Nuclei are stained by Hoechst 33342 (blue). Arrows and arrowheads indicate tdTomato$^+$ activated caspase-3$^+$ and tdTomato$^-$ activated caspase-3$^+$ pyknotic cells, respectively. Proportion of activated caspase-3$^+$ cells in tdTomato$^+$ cells in the GCL of the adult OB is shown (F; 14 dpi, 4/222 cells from three mice; 28 dpi, 0/546 cells from three mice; 56 dpi, 0/767 cells from three mice; pooled from five independent experiments). **(G)** PS exposure at spines of nonapoptotic tdTomato$^+$ granule cells in the adult OB. Representative images of the GCL of the OB in adult *Dcx-CreER^{T2}; R26-tdTomato* mice at 28 dpi (*n* = 3 mice) stained for PS (white) and activated caspase-3 (green). tdTomato$^+$ signals (red) are directly observed without staining. Boxed areas are enlarged in G^1–G^3. Arrowheads and arrows indicate activated caspase-3$^+$ PS$^+$ apoptotic cells and activated caspase-3$^-$ PS$^+$ spines, respectively. None of the tdTomato$^+$ neurons with exposed PS at their spines expresses activated caspase-3 or PS in their soma at 28 and 56 dpi (*n* = 27 cells from three mice at 28 dpi; *n* = 14 cells from three mice at 56 dpi; pooled from four independent experiments). GCL, granule cell layer; EPL, external plexiform layer; ML, molecular layer. Scale bars: A–D, 2 µm; E, 10 µm; G, 5 µm. Data shown are mean ± SEM.

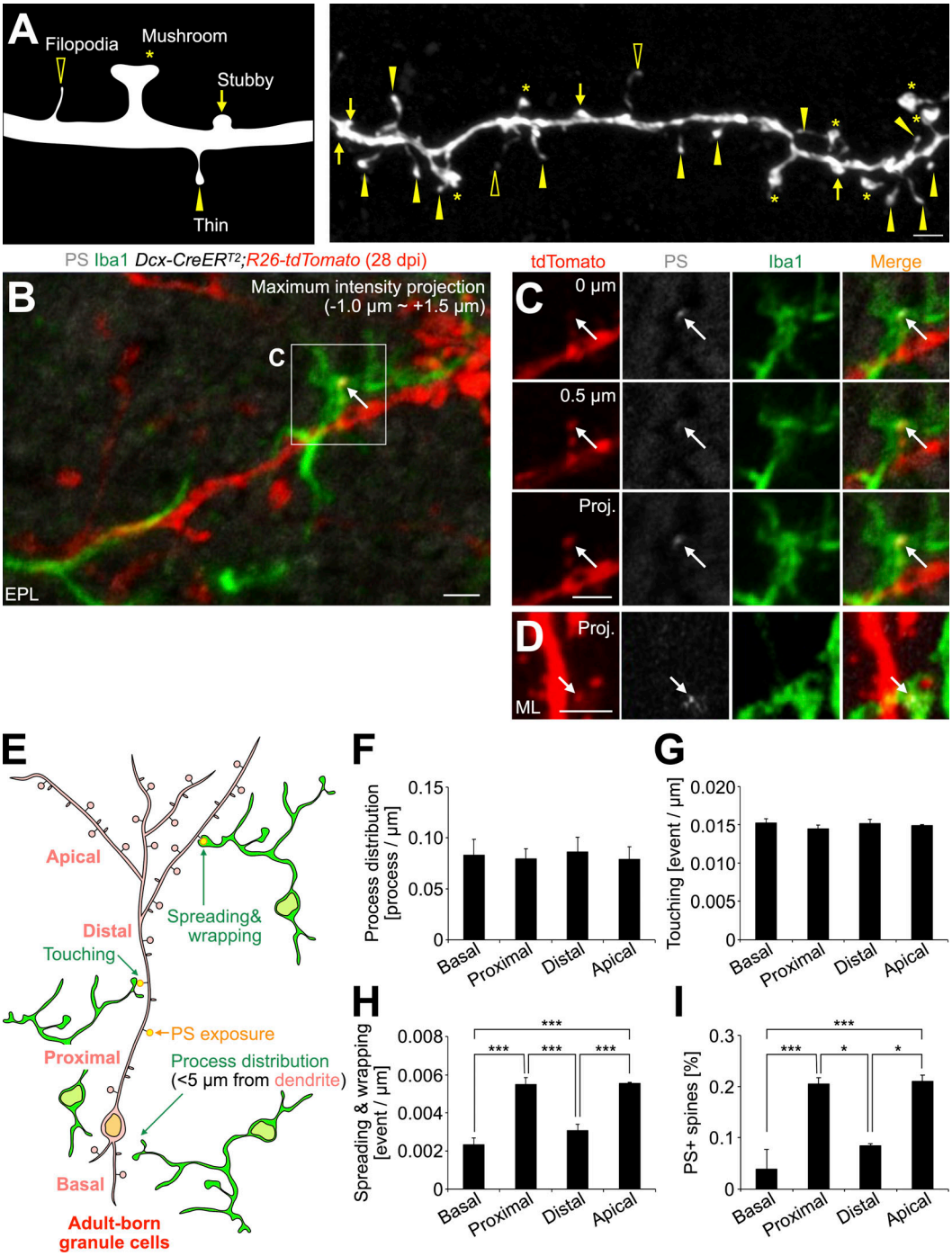

Figure S4. **Subcellular domain-specific regulation of PS exposure and microglial contacts of spines of adult-born neurons. (A)** Classification of spine morphology. Asterisks, mushroom; arrows, stubby; yellow arrowheads, thin; black arrowheads, filopodia. **(B and C)** Representative projection image of the EPL in the OB of adult *Dcx-CreER^{T2}; R26-tdTomato* mice at 28 dpi (n = 8 mice), stained for DsRed (red), PS (white), and Iba1 (green). The boxed area in B is enlarged in C. Arrows indicate a PS$^+$ tdTomato$^+$ thin spine wrapped by Iba1$^+$ microglial process. The two sequential z-planes (0, 0.5 µm) and a projection image (−1.0 to approximately +1.5 µm) of the boxed area in B are shown in C. **(D)** Representative projection image of the DG in the hippocampus of adult *Dcx-CreER^{T2}; R26-tdTomato* mice at 28 dpi (n = 8 mice), stained for DsRed (red), PS (white), and Iba1 (green). Arrows indicate a PS$^+$tdTomato$^+$ spine wrapped by Iba1$^+$ microglia. **(E)** Parameters for microglia–spine interaction (process distribution, touching, spreading and wrapping, and PS exposure). **(F–I)** Densities of microglial process distribution (F, n = 3 mice, pooled from two independent experiments), touching to spines (G, n = 4 mice, pooled from two independent experiments), spreading on and wrapping of spines (H, n = 4 mice, pooled from two independent experiments; $F_{(3,12)}$ = 30.7, P = 0.0000065, one-way ANOVA; basal versus proximal, P = 0.000037, basal versus apical, P = 0.000032, distal versus proximal, P = 0.00048, distal versus apical, P = 0.00040, Tukey–Kramer test), and proportion of PS$^+$ spines (I, n = 3 mice, pooled from two independent experiments; $F_{(3,8)}$ = 16.7, P = 0.00083, one-way ANOVA; basal versus proximal, P = 0.0024, basal versus apical, P = 0.0019, distal versus proximal, P = 0.016, distal versus apical, P = 0.012, Tukey–Kramer test) in the basal, proximal, distal, and apical domains of dendrites of tdTomato$^+$ adult-born granule cells in *Dcx-CreER^{T2}; R26-tdTomato* mice at 28 dpi. EPL, external plexiform layer; ML, molecular layer. Scale bars in A–D, 2 µm. *, P < 0.05; ***, P < 0.005.

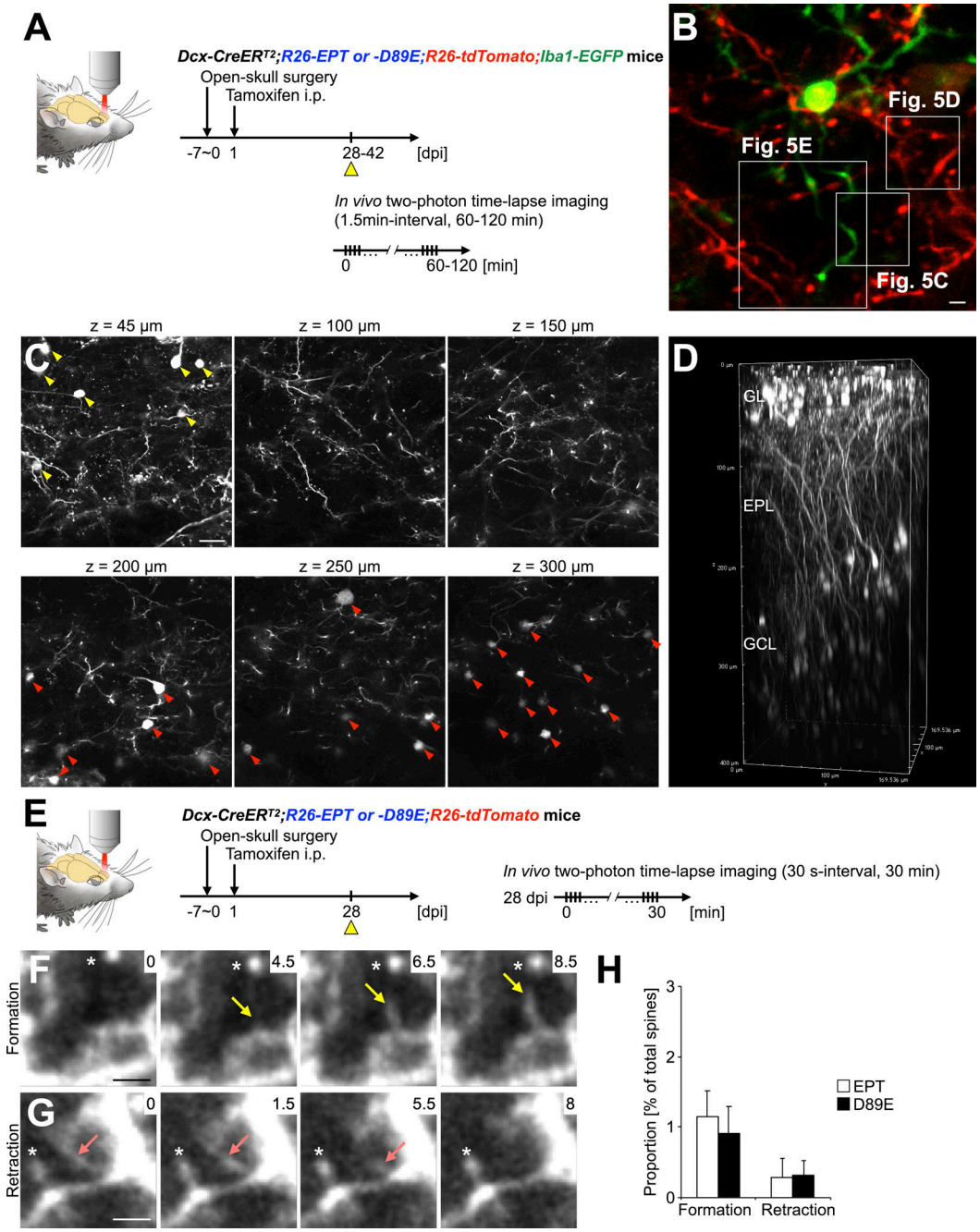

Figure S5. **In vivo two-photon time-lapse imaging of filopodium formation and retraction of adult-born neurons in the OB. (A)** Experimental scheme of in vivo two-photon time-lapse imaging of microglia–spine interaction. **(B)** Representative two-photon image of tdTomato$^+$ dendrites of granule cells (red) and EGFP$^+$ microglia (green) in the EPL of the adult OB. Boxed areas are enlarged in Fig. 5, C–E. Also see Video 4. **(C and D)** In vivo two-photon imaging of dendritic spines of adult-born periglomerular cells and granule cells. Representative z-stack two-photon images (C) and their 3D reconstruction (D) of tdTomato$^+$ periglomerular (yellow arrowheads) and granule (red arrowheads) cells in *Dcx-CreER^{T2}; R26-EPT; R26-tdTomato* (*EPT*) mouse at 28 dpi are shown. **(E)** Experimental scheme of in vivo two-photon time-lapse imaging of filopodium formation and retraction. **(F and G)** Representative in vivo time-lapse images of tdTomato$^+$ filopodium formation (F, yellow arrows) and retraction (G, pink arrows) in the EPL (n = 3 mice, pooled from three independent experiments). Asterisks (F and G) indicate spines stably observed during the whole imaging period. Numbers indicate the time in minutes from the initial image session. **(H)** Frequency of filopodium formation and retraction in the adult *EPT* and *Dcx-CreER^{T2}; R26-D89E; R26-tdTomato* (*D89E*) mice at 28 dpi (n = 3 mice each, pooled from three independent experiments). GL, glomerular layer; EPL, external plexiform layer; GCL, granule cell layer. Scale bars: B, F, and G, 2 µm; C, 20 µm. Data shown are mean ± SEM.

Video 1. 3D reconstruction of microglia in the process of phagocytosis (early) in the adult OB. Microglia (green), granule cells (pink), phagocytosed spine (blue), and mitral cells (light blue) are shown. Also see Fig. 1 C and the 3D interactive model at https://sketchfab.com/3d-models/phagocytosis-of-spine-by-microglia-7f168d4801e1444fb1f14750bbad7175.

Video 2. 3D reconstruction of microglia in the process of partial phagocytosis (early) in the adult OB. Microglia (green), granule cells (pink), phagocytosed spine (blue), and mitral cells (light blue) are shown. Also see Fig. 1 I and the 3D interactive model at https://sketchfab.com/3d-models/partial-phagocytosis-of-spine-by-microglia-b3b4332f1bc74dea86ae81965a3d23d3.

Video 3. Surface-rendered 3D reconstruction of a PSD95$^+$tdTomato$^+$ spine within CD68$^+$ lysosome in Iba1$^+$ microglial process in adult OB. PSD95, tdTomato, CD68, and Iba1 were shown in yellow, red, cyan, and green, respectively. Also, see Fig. 4 G^3.

Video 4. Representative video of in vivo time-lapse imaging of adult-born neurons and microglia in the OB of Dcx-CreERT2; R26-EPT; R26-tdTomato; Iba1-EGFP mice. Dendrites of tdTomato$^+$ adult-born granule cells (red) and EGFP$^+$ microglia (green) were acquired at the interval of 1.5 min for 60.0 min. Video is shown at a rate of 10 frames/s and related to Fig. 5, C–E and Fig. S5 B. Scale bar, 5 µm.

Video 5. Representative video of in vivo time-lapse imaging of adult-born neurons and microglia in the OB of Dcx-CreERT2; R26-D89E; R26-tdTomato; Iba1-EGFP mice. Dendrites of tdTomato$^+$ adult-born granule cells (red) and EGFP$^+$ microglia (green) were acquired at the interval of 1.5 min for 58.5 min. Video is shown at a rate of 10 frames/s and related to Fig. 5 F. Scale bar, 5 µm.

Video 6. Surface-rendered 3D reconstruction of a PSD95$^+$tdTomato$^+$ spine within CD68$^+$ lysosome in Iba1$^+$ microglial process in adult DG. PSD95, tdTomato, CD68, and Iba1 were shown in yellow, red, cyan, and green, respectively. Also, see Fig. 8 D^2.